Incorporation of Sub-Resolution Porosity into Two-Phase Flow Models with a Multiscale Pore Network

Sajjad Foroughi[1*], Branko Bijeljic[1], Ying Gao[1,2], Martin J. Blunt[1]

[1]Department of Earth Science and Engineering, Imperial College London, London, SW7 2BP, United Kingdom

[2]Shell Global Solutions International B.V., Grasweg 31, 1031 HW Amsterdam, Netherlands

Key Points:

- The dilation-based algorithm incorporates sub-resolution porosity as microlinks into the extracted pore network from the resolved pore space. Differential imaging characterizes sub-resolution pore space.
- Empirical model has been used to characterize the flow properties of microlinks.
- The permeability, formation factor, and MICP data were matched by tuning microlink parameters. The tuned multiscale network predicted relative permeability curves.

Corresponding author: S. Foroughi, s.foroughi@imperial.ac.uk

Abstract

Porous materials, such as carbonate rocks, frequently have pore sizes which span many orders of magnitude. This is a challenge for models that rely on an image of the pore space, since much of the pore space may be unresolved. There is a trade off between image size and resolution. For most carbonates, to have an image sufficiently large to be representative of the pore structure, many fine details cannot be captured. In this work, sub-resolution porosity in X-ray images is characterized using differential imaging which quantifies the difference between a dry scan and 30 wt% KI brine saturated rock images. Once characterized, we develop a robust workflow to incorporate the sub-resolution pore space into network model using Darcy-type elements called micro-links. Each grain voxel with sub-resolution porosity is assigned to the two nearest resolved pores using an automatic dilation algorithm. By including these micro-links with empirical models in flow modeling, we simulate single-phase and multiphase flow.

By fine-tuning the micro-link empirical models, we achieve effective permeability, formation factor, and drainage capillary pressure predictions that align with experimental results. We then show that our model can successfully predict steady-state relative permeability measurements on a water-wet Estaillades carbonate sample within the uncertainty of the experiments and modeling. Our approach of incorporating sub-resolution porosity in two-phase flow modeling using image-based multiscale pore network techniques can capture complex pore structures and accurately predict flow behavior in porous materials with a wide range of pore size.

1 Introduction

Two-phase flow in porous media is a critical area in many scientific fields and applications [*Blunt*, 2017; *Sahimi*, 2011; *Bear and Cheng*, 2010; *Zhao*, 2013; *Shokri-Kuehni et al.*, 2017; *Boot-Handford et al.*, 2014; *Juanes et al.*, 2006; *Blunt*, 2022; *Zhang et al.*, 2023c; *Moghadasi et al.*, 2023; *Li et al.*, 2023]. Many porous materials, from electrochemical devices to catalysts and porous rocks, have a wide range of pore size. While three-dimensional imaging, including X-ray micro-tomography (micro-CT) and FIB-SEM, have transformed the characterization of porous media [*Blunt et al.*, 2013; *Meakin and Tartakovsky*, 2009], a single image cannot, in many cases, fully resolve the pore space [*Da Wang et al.*, 2021]. The images themselves form the basis for simulation studies to predict and design the performance of porous structures: this can either be direct simulation of flow and transport in the pore space [*Blunt et al.*, 2013; *Raeini et al.*, 2014; *Akai et al.*, 2019; *Foroughi et al.*, 2018; *McClure et al.*, 2018; *Armstrong et al.*, 2019; *Mostaghimi et al.*, 2013], or network modeling [*Oren et al.*, 2018; *Joekar-Niasar et al.*, 2010; *Raeini et al.*, 2018; *Giudici et al.*, 2023; *Foroughi et al.*, 2020], where the void space is represented by a topologically equivalent lattice of wide regions, pores, connected by constrictions, called throats. However, when the pore space cannot be explicitly resolved, a multiscale modeling approach is required [*Mehmani et al.*, 2013; *Bultreys et al.*, 2015; *Ruspini et al.*, 2021].

Multiscale simulation is a computational strategy that combines the use of the averaged Darcy law with an explicit representation of flow in the pore space [*Brinkman*, 1949]. Multiscale modeling has been employed in direct numerical simulation of porous materials with two characteristic length scales [*Bijeljic et al.*, 2018; *Lesinigo et al.*, 2011; *Guo et al.*, 2018; *Carrillo and Bourg*, 2019] and also extended to multiphase flow [*Dinariev et al.*, 2020; *Wu et al.*, 2022]. Despite its accuracy in predicting fluid flow in complex porous media, it is computationally demanding and resource-intensive [*Meakin and Tartakovsky*, 2009; *Raeini et al.*, 2012].

In contrast to direct numerical simulation, pore network modeling is more computationally efficient [*Øren et al.*, 2019; *Foroughi et al.*, 2020, 2021; *Bultreys et al.*, 2018; *Raeini et al.*, 2019; *Giudici et al.*, 2023]. However, for materials, such as carbonate rocks, with a significant fraction of the pore space that is unresolved by micro-CT imaging, which are the subject of the current study, multiscale image-based models must be developed, validated, and tested. The use of network models allow many simulations to be run efficiently while capturing displacement behavior over a wide range of length scales.

Various methodologies to construct and simulate flow through multiscale pore networks have been proposed in the literature. These methods can be classified into two general groups: the first group generates a network where pores and throats at two distinct scales are explicitly incorporated. The smaller elements are captured using ultra-high-resolution imaging (such as nano-CT) and merged with pores and throats imaged, for instance, using micro-CT scanning [*Mehmani et al.*, 2013; *Mehmani and Prodanović*, 2014; *Prodanović et al.*, 2015; *Jiang et al.*, 2013; *Bekri et al.*, 2005]. The second group replaces regions of the pore space where a single image is unable to explicitly resolve pores with Darcy-type elements whose properties are some appropriate average over many smaller elements [*Bauer et al.*, 2011, 2012; *Bultreys et al.*, 2015, 2016; *Ruspini et al.*, 2021; *Wang et al.*, 2022].

Generating synthetic pore networks, which explicitly represent pores and throats over multiple scales, has some drawbacks, including potential inaccuracies in representing the actual pore structure, difficulties and uncertainties in fusing synthetic and micro-CT extracted networks, and the possibility of time-consuming and computationally expensive network modeling due to the increased number of elements. Instead, the use of effective Darcy-like elements that consider the averaged behavior of several combined small-scale elements is more computationally efficient. The problem is how to characterize their properties. One method, used in this paper, is differential imaging which can at least capture locally the connected porosity of unresolved elements [*Lin et al.*, 2016].

Multiscale network models, which represent sub-resolution porosity as a continuous medium or Darcy element, have been used in several studies. *Bauer et al.* [2011, 2012] introduced a Darcy-type throat between two pores only when a macro-throat (a throat that is explicitly resolved in the underlying image) already existed between them. While these works successfully captured micro-porosity as a parallel circuit along the macro-pore throats, they inherently assumed that connectivity through micro-porosity only occurs where there is connectivity through resolved macro-throats. This assumption might limit their models' ability to accurately represent the behavior of complex porous media, particularly when the micro-porous regions provide additional connectivity and accessibility that are not captured by the resolved macro-throats.

This limitation was later addressed by *Bultreys et al.* [2015], who extended Bauer's approach to include Darcy connections between pores regardless of the presence of macro-throats. They tested their model by extracting a multiscale network from an Estaillades micro-CT image and compared it to the drainage relative permeability measurement from the study by *Ott et al.* [2015]. In a subsequent study, they compared the waterflooding results for Estaillades limestone with experimental results for

a Middle Eastern carbonate reservoir rock [*Bultreys et al.*, 2016]. Later *Wang et al.* [2022] used the same approach to create a pore network model that effectively handles complex, multiscale porosity. This approach shows promise in addressing sub-resolution porosity using micro-links (connections between explicitly resolved macro-pores). However, they did not validate their multiscale results for waterflooding in Estaillades against experimental data from the same sample. Additionally, their methodology does not guarantee the exclusive assignment of each sub-resolution voxel to a specific micro-link. Moreover, there is an artificial constraint on the allowed maximum length of a micro-link. In our study, we address these issues by developing a generative algorithm for micro-link characterization and proposing a methodology to incorporate wettability in empirical models for micro-links. Then we successfully validate our methodology against a waterflooding experiment on Estaillades.

Recently, *Ruspini et al.* [2021] introduced a multiscale digital rock workflow. They used Darcy-type pores for unresolved porosity and considered connections through additional micro-porous micro-throats (without length and volume). They represented smaller-scale pore structures in a continuum manner using relative permeability and capillary pressure saturation functions calculated from high-resolution images. The multiscale workflow incorporates experimental data to constrain modeling assumptions at different scales. The workflow was validated using two complex reservoir rocks, and the numerical predictions showed good agreement with the experimental data. However, the main concern lies in the generalizability of the high-resolution imaging data. While the researchers were able to derive information from high-resolution images for specific areas, this local information may not be representative of the whole sample. Furthermore, the study relies heavily on high-quality imaging, such as sub-micron resolution images, which might not be easily accessible or feasible in all situations. Finally, wettability is assigned to micro-porous regions by matching to the measured waterflood capillary pressure which requires additional experimental information.

While existing studies effectively address unresolved porosity in complex porous media, a need persists for a more automated and robust algorithm for characterizing sub-resolution elements and incorporating them into a model with explicitly resolved pores and throats. In addition, the general relations for micro-links should consider diverse constraints, such as geometry and wettability, and be supported by experimental data for both single and two-phase flow. It is important to create a standard, automatic workflow that can be used for every micro-CT experiment involving sub-resolution porosity without needing to adjust the geometrical parameters every time. Another crucial question is how to reduce the amount of experimental work needed to gather enough data for the

multiscale model. If too much effort is required to collect the experimental data used as input, it might be more cost-effective to directly measure relative permeabilities.

In response to these needs, we have developed a workflow that incorporates sub-resolution porosity from differential imaging into pore network modeling, thus establishing a robust multiscale approach. Unlike previous work, our method incorporates a dilation algorithm to automatically identify micro-links between macro-pores, guaranteeing each accessible micro-porous voxel is assigned to a specific micro-link. This eliminates the need for arbitrary constraints on the micro-link length and maintains model efficiency without compromising the accurate representation of the complex pore structure. The following items distinguish the algorithm developed in this paper from previous studies:

1. Based on dilation, we have developed an automatic and robust algorithm that allows us to consider sub-resolution porosity as micro-links that connect the two nearest resolved pores and construct a multiscale pore network.
2. Considering sub-resolution porosity as micro-links, similar to resolved throat elements, means the number of linear equations in the multiscale pore network will be the same as in the resolved network (i.e., the same number of pores). This is in contrast to methods that consider this sub-resolution porosity as a type of pore element, resulting in a larger set of equations to solve for flow calculations.
3. Based on our capillary model proposed for all types of wettability, it is possible to derive scanning curves with minimal information regarding the wettability of the system. This eliminates the need for experiments to derive scanning capillary pressure data .

We apply our model to Estaillades carbonate using primary drainage capillary pressure data to calibrate the geometric parameters in the model.

The structure of this paper is as follows: Section 2 briefly describes the imaging experiment performed on Estaillades carbonate, which serves as a validation experiment. We then elaborate on our workflow for incorporating sub-resolution porosity into pore network modeling. In Section 3, we first assess the sensitivity of the multiscale approach and then validate its results against experimental data. Finally, Section 4 concludes the paper with a summary and discussion of future work.

2 Materials and Methods

Gao et al. [2019] conducted a study to investigate the behavior of pore occupancy, relative permeability, and flow intermittency measurements using X-ray micro-tomography in a complex carbonate Estaillades sample. The experiment specifically focused on a high capillary number, $Ca = 7.3 \times 10^{-6}$, which was intentionally chosen to examine the effect of flow intermittency, where the configuration of the phases fluctuates.

Concurrently, a hitherto unpublished experiment was performed on a different Estaillades sample that had a significantly lower capillary number (2.1×10^{-7}). In this experiment, the displacement was capillary-dominated with a fixed configuration of phases during steady-state flow. It was conducted on a water-wet Estaillades sample and followed a similar procedure to the high capillary number experiment.

Given its absence of dynamic effects, its water-wet condition, and its notable sub-resolution porosity that has been characterized through differential imaging, this second, unpublished experiment is deemed an ideal case for validating our multiscale quasi-static pore network methodology. Subsequent sections will provide a brief overview of the experimental materials, procedures, and analysis. Furthermore, a link to the images obtained from the experiment can be found at the end of the paper. For a more comprehensive understanding of the experimental procedures and analysis methods, readers are encouraged to refer to the work by *Gao et al.* [2019]; *Lin et al.* [2021].

2.1 Rock and fluid properties

The sample used in this study is Estaillades carbonate. It was cylindrical, with a diameter of 6.00 ± 0.01 mm and a length of 46.70 ± 0.01 mm. A companion sample was composed of approximately 97.9% calcite and 2.1% quartz, as analyzed at Weatherford Laboratories in East Grinstead, UK [*Gao et al.*, 2019].

Using Darcy's law and pressure differential measurements at three flow rates (0.1 mL/min, 0.3 mL/min, and 0.6 mL/min), corresponding to pressure drops in the sample of 25.76 kPa, 80.81 kPa, and 166.60 kPa respectively, and corresponding pressure drops in the tubing without the sample of 4.30 kPa, 12.91 kPa, and 25.83 kPa, the absolute permeability of the sample was calculated to be 128 ± 4 mD. The uncertainty in the permeability was determined using the Monte Carlo method, considering uncertainties of 0.1% in measured pressure, 0.5% in flow rates, 0.01 mPa·s in viscosity, and 0.01 mm in the length and diameter of the sample.

The total porosity, estimated from the micro-CT image in Section 2.3, was 28.2 ± 1.5%, with micro-porosity and macro-porosity accounting for 19.0% and 9.2% respectively. The reported helium porosity for another Estaillades sample was 30.3 ± 0.2%. The image-based porosity value for both this sample and the other Estaillades sample is slightly lower than the helium porosity suggesting that some micro-porosity might not have been captured.

The non-wetting phase was decane, with a density of 730 kg/m^3 (n-Decane, Acros Organics) and a viscosity of 0.838 mPa·s (provided by PubChem, open chemistry database). To achieve optimal contrast between the brine, oil, and rock phases, a 30 wt% potassium iodide (KI) brine was used as the wetting (aqueous or brine) phase. The density of brine was measured to be 1263 ± 2 kg/m^3 at ambient conditions by weighing a 1 mL drop of the liquid. The viscosity of the brine was determined to be 0.82 ± 0.01 mPa·s.

The interfacial tension between brine and decane was measured using the pendant drop method [*Andreas et al.*, 2002; *Stauffer*, 1965], yielding a value of 47 ± 2 mN/m at ambient conditions, as determined by a Ramé-Hart apparatus (590 F4 series).

2.2 Experimental procedure for *in situ* X-ray tomography

Our experiment utilized a 1 *mm* thick, X-ray transparent Hassler-type flow cell made from carbon fiber epoxy specially designed to withstand high pressures while remaining nearly transparent to X-rays. The cylindrical Estaillades sample was positioned within this cell, encased within a Viton sleeve, and connected to the fluid flow-lines via metal fittings. Simultaneous injection of brine and decane was performed through separate ports at a maintained total flow rate of $0.02\,mL/min$ corresponding to a linear flow velocity of $0.71\,mm/min$. We used this total flow rate and the mean viscosity value of oil and brine to calculate the capillary number, obtaining a value of 2.1×10^{-7}. This categorized our experiment within the capillary dominant regime, common to reservoir settings. The ratio of the Darcy velocity of the aqueous phase to the total velocity of both oil and aqueous phases ($f = \frac{q_w}{q_t}$) defines the fractional flow. In the course of the experiment, we increased the fractional flow sequentially to reach steady-state at the following values: 0, 0.15, 0.3, 0.5, 0.7, 0.85, and 1. For further details on the experimental design, refer to the published work by *Gao et al.* [2019].

The experimental procedure was akin to other studies on intermittency by *Gao et al.* [2019]. The steps taken are explained in further detail in the Appendix Section 5.1.

We imaged the fluid configurations using a Zeiss XRM-510 X-Ray microscope. The process employed a flat panel detector, achieving a voxel size of 3.58 μm. It involved an X-ray energy of 75 keV, an exposure duration of 0.5 seconds, and 1601 projections. These projections were converted into a three-dimensional image using the proprietary software of the Versa system. To broaden the vertical (flow direction) field of view for analysis, two images were captured, stitched together, and cropped into cylindrical forms to remove the sleeve visible at the core boundaries. The final image had dimensions of $1608 \times 1598 \times 2720$ voxels (5.76 mm in diameter and 9.74 mm in length), representing a total volume of 252.1 mm^3. To ensure a uniform orientation, all the reconstructed images were registered to the dry scan image. The resampling of these images was facilitated by the Lanczos algorithm [*Burger and Burge*, 2022].

2.3 Image Analysis and Determination of Macroscopic Parameters

2.3.1 Characterization of Micro- and Macro-pore Space

The Estaillades carbonate exhibited a bimodal pore structure with inter-granular macro-porosity and micro-porosity. Mercury injection capillary pressure, MICP, analysis showed two peaks in the throat radius distribution at around 0.2 and 10 μm [*Tanino and Blunt*, 2012; *Bijeljic et al.*, 2013; *Alyafei and Blunt*, 2016].

Images were segmented into grains, resolved pores, and sub-resolution pore spaces; the use of 30 wt% KI brine intensified the contrast and emphasized sub-resolution porosity [*Lin et al.*, 2016]. Commercial software, Avizo, was used for image analysis, segmenting the images into resolved, sub-resolution pore space and grains using the interactive thresholding segmentation method. Differential imaging facilitated the discrimination of sub-resolution porosity within the images, enabling the separation of voxels solely filled with brine, voxels partially filled with brine representing the sub-resolution pore space, and voxels constituting grain without any sub-resolution porosity. Figure 1 represents histograms of grayscale CT numbers or intensity values, indicative of X-ray attenuation, for the various phases. These histograms allow for the distinct identification of solid grain, resolved pore, and voxels containing sub-resolution porosity.

Dry and saturated scans, illustrated in Figures 2a and 2b, respectively, leveraged brine's high X-ray adsorption for clear imaging. Differential imaging then enabled the discrimination of micro and macro-porosity. A non-local means filter was applied to the differential images to reduce noise [*Buades et al.*, 2005, 2008], and intensity-based thresholding segmented the image into distinct phases [*Lin et al.*, 2016] (see Figure 2d).

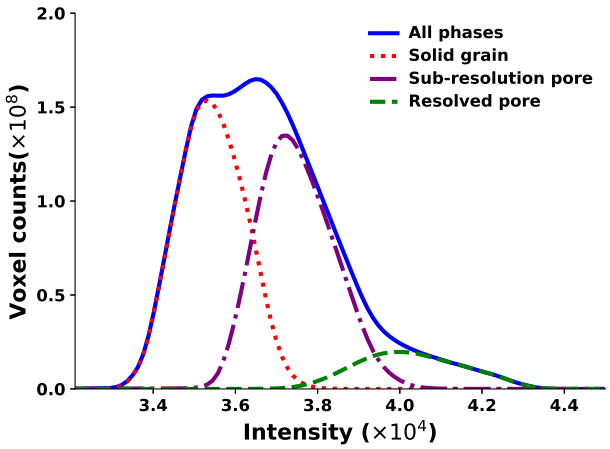

Figure 1. Histograms of intensity for different phases obtained from the brine-saturated scan. Each line represents a specific phase found in the scan, including the 'All phases', category.

In the context of a dry scan, the average intensity $\bar{I}_{\text{dry}}$ is related to the porosity (ϕ) and the specific intensities of air (I_{air}) and rock (I_{rock}):

$$\bar{I}_{\text{dry}} = \phi I_{\text{air}} + (1 - \phi) I_{\text{rock}} \tag{1}$$

For a brine-saturated scan, the average intensity $\bar{I}_{\text{brine}}$ is a function of the porosity and the intensities of brine and rock:

$$\bar{I}_{\text{brine}} = \phi I_{\text{brine}} + (1 - \phi) I_{\text{rock}} \tag{2}$$

Porosity is determined by the difference in average intensity between the brine-saturated scan and the dry scan, normalized by the difference in specific intensities of brine and air:

$$\phi = \frac{\bar{I}_{\text{brine}} - \bar{I}_{\text{dry}}}{I_{\text{brine}} - I_{\text{air}}} \tag{3}$$

This approach essentially measures the contrast change in the image due to the replacement of air by brine in the pore space.

For saturation, the formula is based on the average intensity of a fluid mixture scan $\bar{I}_{\text{f}_w}$. It is computed by accounting for the porosity, water saturation (S_w), and the specific intensities of brine, oil, and rock:

$$\bar{I}_{\text{f}_w} = \phi S_w I_{\text{brine}} + \phi(1 - S_w) I_{\text{oil}} + (1 - \phi) I_{\text{rock}} \tag{4}$$

The water saturation is then calculated from the difference in average intensity between the brine-saturated scan and the fluid mixture scan, normalized by the difference in specific intensities of brine

and oil:

$$S_w = 1 - \frac{\bar{I}_{\text{brine}} - \bar{I}_{\text{f}_w}}{\phi(I_{\text{brine}} - I_{\text{oil}})} \tag{5}$$

This process essentially quantifies the contrast change due to the partial replacement of brine by oil.

Importantly, we normalize the images to have the same intensity for rock in brine-saturated, dry, and fluid mixture images and also the same intensity for brine in both brine-saturated and fluid mixture images. This ensures consistent interpretation of image intensities across different scans and conditions. Taking into account the uncertainty inherent in determining the intensity of phases allows us to estimate the resulting uncertainty in the calculated values of porosity and saturation.

2.3.2 Relative Permeability and Uncertainty Quantification

As mentioned above, the pressure difference across the rock sample at steady-state conditions was measured using the differential pressure transducer. We recorded the mean pressure differentials at different fractional flows during the last two hours, as well as the corresponding standard deviation. We subtracted the pressure drop in the flow lines themselves (see step 10 of the experimental procedure in the Appendix Section 5.1). The relative permeability was calculated by:

$$k_{rw} = \frac{q_w \mu_w L}{K \Delta p}; \quad k_{ro} = \frac{q_o \mu_o L}{K \Delta p} \tag{6}$$

k_{rw} and k_{ro} represent the relative permeabilities of water and oil, respectively. q_w denotes the Darcy velocity of brine (flow rate per unit area) in m/s, while q_o denotes the Darcy velocity of oil in m/s.

The parameters μ_w and μ_o signify the viscosities of water and oil respectively, measured in units of Pa·s. The term L represents the length of the porous medium through which fluid flow occurs, quantified in meters. Δp, denoting the pressure drop across the sample, is expressed in Pascals. K is the absolute permeability (m^2) determined from single-phase flow (water) through the porous medium based on Darcy's law:

$$K = \frac{q_t \mu_w L}{\Delta p}; \tag{7}$$

where q_t is the Darcy velocity for single-phase flow, also measured in meters per second (m/s).

It is important to note that the pressure drops in Eqs. 6 and 7 are corrected by excluding the pressure drop across the tubing in the absence of the sample. Uncertainties are computed by considering the variability in all these parameters. Additionally, to accommodate the impact of local fluctuations in the average saturation in the flow direction, an adjustment is made to the relative permeability according to the methodology proposed by *Zhang et al.* [2023a] and *Zhang et al.* [2023b].

2.4 Modeling

2.4.1 Brief Introduction to Pore Network Modeling (PNM)

In this section we will introduce quasi-static pore network modeling based on our previous work [*Blunt et al.*, 2002; *Valvatne and Blunt*, 2004]; later we will describe the extensions implemented to accommodate micro-porosity. A pore network simplifies the representation of a porous medium as a network of pores and throats. This streamlined representation is accomplished using the maximal ball method, which identifies pores as local maxima from the distance map of the nearest solid, while throats are defined as narrow passageways connecting two neighboring pores. Comprehensive details on the pore network extraction workflow can be found in the following references [*Dong and Blunt*, 2009; *Raeini et al.*, 2017]. The software used for this extraction, referred to as *pnextract*, is available through the GitHub link provided at the end of this paper. The primary advantage of simplifying intricate pore structures into a network of pores and throats is the facilitation it offers for fluid flow simulation. The code to simulate multiphase flow assumes capillary-controlled displacement and has two main steps. First, we determine the distribution of fluid phases at a specific pressure for the invading phase. Then, we calculate the pressure or potential field in the pore network by solving the mass or current balance equations for each phase.

Gradually increasing the pressure of the invading phase at the inlet leads to updates in the fluid-fluid interface locations. These updates cause changes in the distribution or saturation of the fluid phase in the network. Displacements of the fluid phase within the center of the element can occur due to potential invasion events, such as piston-like displacement, snap-off, or pore body filling. They can also happen as the fluid interface moves within each individual element, aiming to reach a new equilibrium state. These changes ultimately affect the curvature of the interface, which balances the pressure difference between the phases,

$$P_c = P_2 - P_1 = \sigma\kappa \tag{8}$$

where P_c is the capillary pressure, P_1 and P_2 are the fluid pressures of the two phases (phase 1 is brine and phase 2 is oil), σ is the interfacial tension, and κ is the total curvature of the interface. When the pressure difference exceeds the capillary pressure required for a specific event (psiton-like displacement, pore body filling, snap-off) in the pore or throat, the event occurs [*Blunt*, 2001; *Blunt et al.*, 2002; *Valvatne and Blunt*, 2004].

For a known distribution of phases, volume conservation is imposed at each pore, assuming incompressible fluids:

$$\sum_j Q_{p,ij} = 0 \quad \forall i \tag{9}$$

where j runs over all throats connected to pore i. The flow rate, Q (volume per unit time), between each pair of neighboring pores i and j is determined by multiplying the conductance between the two pores by the pressure difference between them.

$$Q_{p,ij} = \frac{g_{p,ij}}{L_{ij}}(P_i - P_j) \tag{10}$$

where P is pressure, g_p is fluid conductance, and L is the length between the pore centers. The conductance represents the inverse of the resistance, which is the sum of the resistance of two pores and the connecting throat. Conductance is controlled by the geometrical parameters of pores and throats [*Blunt*, 2001; *Blunt et al.*, 2002; *Valvatne and Blunt*, 2004], which are determined from the image:

$$\frac{L_{ij}}{g_{p,ij}} = \frac{L_i}{g_{p,i}} + \frac{L_t}{g_{p,t}} + \frac{L_j}{g_{p,j}} \tag{11}$$

where t indicates the connecting throat. The pore lengths, L_i and L_j are the lengths from the pore-throat interface to the pore center and L_t is the length of throat measure the length between the pore-throat interface i and pore-throat interface j.

Eq. (9) leads to a system of linear equations for pressure. Solving this system enables us to determine the flow rate for each phase and, subsequently, calculate the permeability for that phase. A similar system of equations can also be used to compute the electrical current through the pore space in response to a potential gradient, invoking conservation of charge. The equations are identical in form, but g represents the electrical conductivity, Q is the current and P the electrical potential.

2.4.2 Development of the Multiscale Pore Network Modeling Workflow - Topology Update

We assume that any voxel with sub-resolution porosity—whether directly connected to the pore space or through other sub-resolution pores—should be included in the multiscale pore network and considered during the micro-link identification process. We present a comprehensive, automatic algorithm in the following sections, developed to effectively incorporate these micro-links into the pore-scale flow model.

The workflow is illustrated in Figure 2. Traditional image-based pore network modeling relies on segmented images from dry scans, with extracted networks composed of pores and throats. The first row in Figure 2 illustrates this process, where (a) is the dry scan image, (c) is the segmented dry

scan image, and (e) shows the topology of the extracted network. Even for rocks with permeability of 100s of miilidarcies some pores and throats may not be fully resolved however [*Leu et al.*, 2014; *Saxena et al.*, 2017, 2019].

However, since in the workflow we propose to include sub-resolution porosity, we acquire an additional image using high concentration brine as shown in Figure 2 (b). Using differential imaging and Figure 2 (a) and (b), we distinguish voxels with sub-resolution porosity from solid voxels and determine the porosity of each voxel (see Figure 2 (d)).

These voxels with sub-resolution porosity should be incorporated into the extracted network shown in Figure 2 (e). This is accomplished using the detailed workflow that will be described later, considering a new element called a micro-link. This results in a multiscale network as shown in Figure 2 (f).

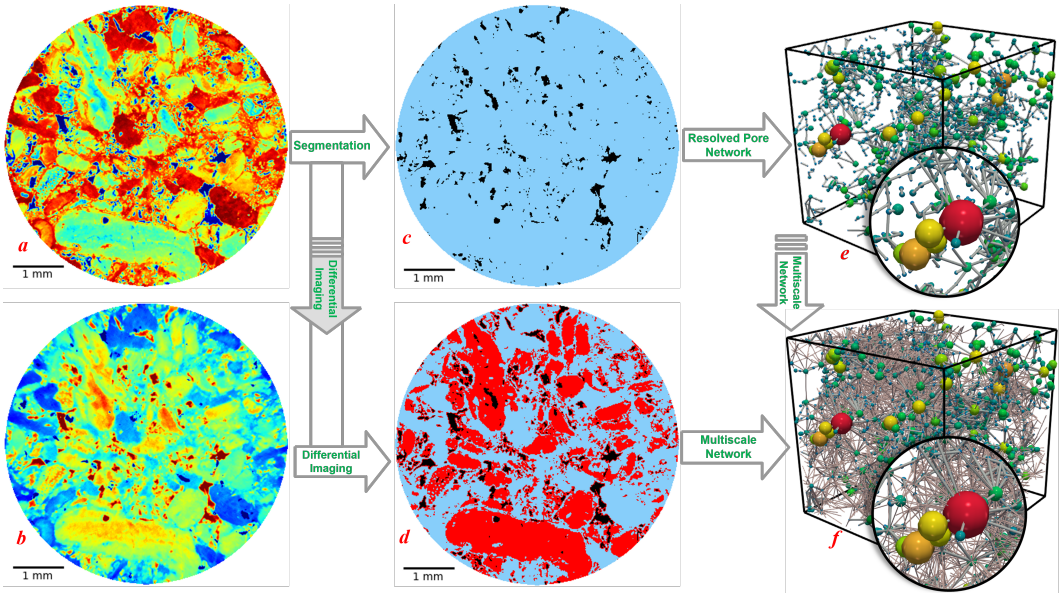

Figure 2. (a) Displays a 2D slice from a dry-scan 3D image used to identify resolved pore space. The different colors represent the density of each phase. In the wet image, red represents the highest density (grains), green represents the intermediate phase (microporous regions), while blue represents the resolvable pore space. In the dry image, it is the other way around.(b) Presents the same 2D slice as in (a), but of the rock saturated with 30% KI brine. This image is used alongside (a) for differential imaging to discern solid voxels containing sub-resolution porosity. (c) Features the same slice as (a) after watershed segmentation, highlighting resolved pores in black for conventional pore network extraction. (d) Depicts the same slice as in (a), (b), and (c), but segmented to label three components: resolved pore voxels (black), solid voxels (blue), and voxels containing sub-resolution porosity (red), which are distinguished through differential imaging. The porosity of the red voxels is determined using the grayscale values from (a) and (b). (e) Presents a 3D schematic of the network, composed of macro-pores and macro-throats, extracted from the resolved pores (c). (f) Shows the schematic of a multiscale pore network, which incorporates the extracted network from (e), the pore label image generated by network extraction (not shown here), and the 3D image from (d). This facilitates the identification and characterization of micro-links, resulting in a network composed of macro-pores, macro-throats, and additional micro-links.

2.4.2.1 **Development of An Automatic Algorithm for Micro-link Identification:** We treat voxels with sub-resolution porosity as micro-links connecting two resolved pores, provided that these pores are interconnected via these micro-links. The fundamental hypothesis of our workflow involves identifying the two nearest accessible pores for each voxel with sub-resolution porosity, a task accomplished through an automated dilation algorithm.

The first step in this process involves assigning a pore label to each void voxel during pore network extraction. The output of this stage is a pore labeling map that assigns each void voxel to a specific pore (e.g., as seen in the first column of Figure 4, where schematically (a) and (b) display pores differentiated by various colors. The gray area represents voxels with sub-resolution porosity).

During network extraction, the local maxima of the void space are assigned a pore label. The *pnextract* code then assigns these pore labels to all nearby void voxels, up to a boundary corresponding to the throat surface. This procedure results in a field map of pore labels for void voxels, which is approximately the same size as the dry scan image. This field map is then used to assign the two nearest pore labels to solid voxels containing sub-resolution porosity. This is done using a dilation algorithm in which, the pore labels start to grow into neighboring solid with sub-resolution voxels, and this process continues until each voxel with sub-resolution porosity has two pore labels assigned. the process schematiclly descirbed in Fig. 3.

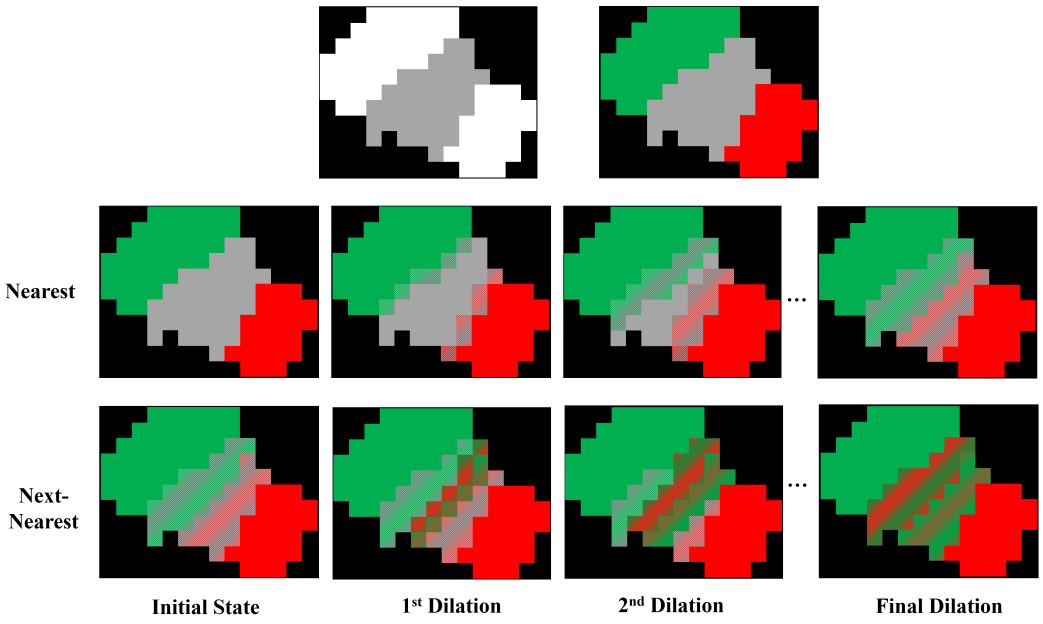

Figure 3. Schematic of the dilation algorithm. The first row represents a porous medium in which white represents void, gray represents voxels with sub-resolution porosity, and black represents solid rock with no porosity. The pore network extraction identifies two pore labels for void voxels. The second row explains the steps taken using the dilation algorithm to identify nearest pores, and the third row explains the steps to identify next-nearest pores.

The explanation of this process in more detail is as follows:

- ***Assigning Nearest Pore Labels to Voxels with Sub-Resolution Porosity—An Algorithmic Approach:*** The process of identifying micro-links starts with assigning the two nearest pore labels to each grain voxel that contains sub-resolution porosity, a process carried out in two stages using dilation algorithms.

  In the initial stage, we create a matrix, *microPore1*, that is the same size as the pore-label matrix. Void voxels are initialized to correspond with the pore label matrix, while all other voxels (grains with or without sub-resolution porosity) are set to zero. We use another matrix to identify grain voxels with sub-resolution porosity. A schematic representation of cases in which we have two or three pores with a gray area (the region with sub-resolution porosity) in between is shown in the first columns of Figure 4 (a) and (b), respectively.

  Applying a dilation algorithm, we extend the *microPore1* pore label to adjacent grain voxels containing sub-resolution porosity, thereby updating *microPore1*. The first layer of voxels with sub-resolution porosity that directly contacts the pore inherits the adjacent void voxel's pore label, signifying the nearest pore label. This action updates the *microPore1* matrix.

  The dilation process is performed randomly across six directions to prevent directional bias. This process only applies to voxels with sub-resolution porosity. Grain voxels without sub-resolution porosity are not part of the dilation process.

  This procedure is repeated, updating the *microPore1* matrix through subsequent dilation levels until no more changes occur. By this stage, all grain voxels containing sub-resolution porosity that are directly accessible to void space or through other microporous voxels will have been assigned the nearest pore label. The output of this process for cases in which we have two and three pores and a gray area (the region with sub-resolution porosity) in between is shown in the second columns of Figure 4 (a) and (b), respectively.

- ***Assigning Next-Nearest Pore Labels to Voxels with Sub-Resolution Porosity—An Algorithmic Approach:*** The second step involves assigning the next-nearest pore label to each grain voxel with sub-resolution porosity. We use a similar algorithm as before. We initialize a new matrix, *microPore2*, of the same size as *microPore1*, with all elements initially set to zero. We then dilate *microPore1* and assign the results to *microPore2*. Dilation occurs through void voxels and grains with sub-resolution porosity. The dilation of *microPore2* continues through the void voxels and grains with sub-resolution porosity until no further changes occur in *microPore2*. After these two steps, we obtain two matrices, each the same size as the dry scan image, in which each voxel with sub-resolution porosity is associated with its nearest and next-nearest pore, as indicated by *microPore1* and *microPore2*, respectively.

A schematic representation of next-nearest pores for cases where we have two or three pores with a gray area (the region with sub-resolution porosity) in between is shown in the third columns of Figure 4 (a) and (b), respectively.

- ***Identification of Micro-Links:*** Once we have successfully assigned two labels to each grain voxel with sub-resolution porosity—either in direct contact with a void voxel or connected through other voxels with sub-resolution porosity—we can identify the micro-links. A micro-link comprises all grain voxels with sub-resolution porosity that share the same pair of labels, regardless of their order. In other words, all elements in the *microPore1* matrix with label *i*, and corresponding elements in the *microPore2* matrix with label *j* (or vice versa), correspond to a micro-link *m* that connects Pore *i* and Pore *j*. A schematic representation of a micro-link between adjacent pores, determined after superimposing *microPore1* and *microPore2* on each other for cases where we have two or three pores with a gray area (the region with sub-resolution porosity) in between, is shown in the fourth columns of Figure 4 (a) and (b), respectively. We then assign the parameters of micro-link *m* based on these grouped voxels. Note that many microporous voxels will be assigned to the same micro-links: the number of micro-links is therefore much smaller than the number of voxels in the image.

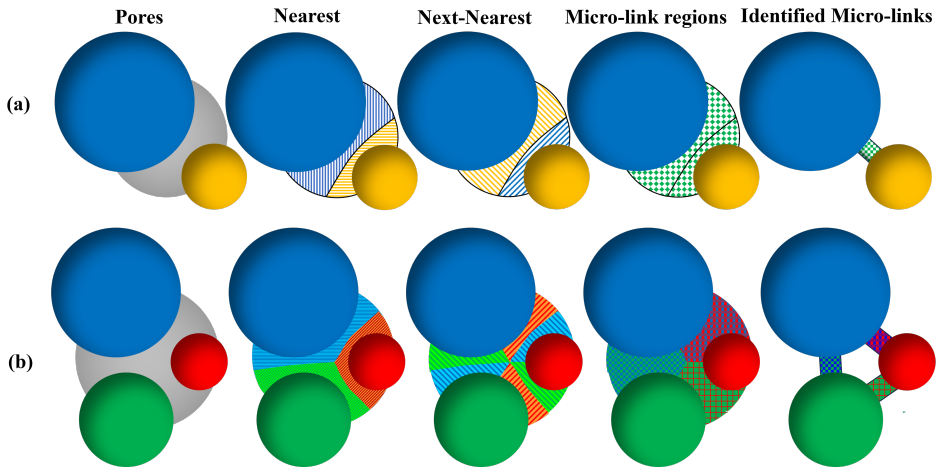

Figure 4. The first column presents a schematic of resolved pores with a gray area denoting the voxels that connect these pores via sub-resolution porosity. The first row consists of two pores, while the second row contains three. The identification of these pores is facilitated by a pore network extraction on the resolved pore space. The second column highlights the use of the dilation algorithm, which assists in recognizing the nearest pore label for each voxel with sub-resolution porosity. With further dilation, we can identify the next-nearest pore label for each voxel with sub-resolution porosity, as illustrated in the third column. The fourth column demonstrates the process of superimposing the nearest and next-nearest labels, enabling the identification of micro-links. Each voxel sharing the same set of nearest and next-nearest labels, irrespective of order, corresponds to a unique micro-link.

2.4.2.2 **Addressing Computational Challenges in the Proposed Algorithm:** The dilation algorithm poses substantial computational challenges, particularly when processing large images. To mitigate this issue, we implemented a strategy that subdivides the label matrix into smaller sub-matrices. The computations for each of these sub-matrices are executed concurrently using multi-threading, significantly enhancing the efficiency of the algorithm. By employing this strategy, we successfully navigated the computational complexity associated with the dilation algorithm, enabling the processing of large images without encountering excessive computational costs.

2.4.2.3 **Integrating Micro-Links into the Resolved Pore Space-Derived Network and Redefining Topology:** A traditional pore network, derived from resolved pore space, comprises pores and throats. In this context, pores represent larger void spaces within porous media, while throats function as connecting constrictions.

For illustrative purposes, we have provided an example topology from a pore network. This network has been extracted from the resolved pore space of Estaillades rock and is depicted in Figure 5(a). Additionally, Figure 5(b) presents the updated network structure incorporating micro-links, often referred to as the multiscale pore network model.

The incorporation of micro-links as a new element in this framework, and the corresponding update to the network topology, require modifications to the output files generated by the *pnextract* code. These amendments account for a new throat type and adjustments to the coordination numbers of the pores.

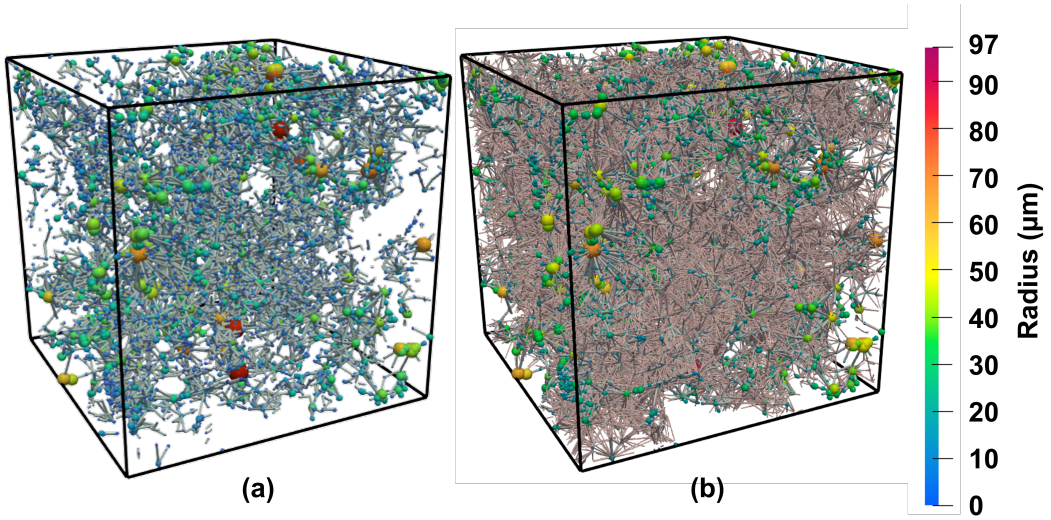

Figure 5. (a) Topology of the extracted pore network based on the resolved pore space. (b) Updated topology of the same pore network after incorporation of micro-links (referred to as the multiscale pore network).

2.4.3 Development of the Multiscale Pore Network Modeling Workflow - Flow Modeling Update

2.4.3.1 **Characterization of Micro-Links:** Consider a micro-link, denoted m, connecting pores i and j. Consider a voxel with index k with sub-resolution porosity corresponding to this micro-link. The porosity of this voxel is given by $\phi_k^{(m)}$. Therefore, the porosity of the micro-link, denoted as ϕ_m, is defined as:

$$\phi_m = \frac{\sum_k^{N_m^{\text{voxels}}} \phi_k^{(m)}}{N_m^{\text{voxels}}} \tag{12}$$

where N_m^{voxels} represents the number of voxels with sub-resolution porosity associated with micro-link m. The total volume of the micro-link, denoted as V_m^T, is equal to the total volume of the

corresponding voxels:

$$V_m^T = dx^3 N_m^{\text{voxels}} \tag{13}$$

where dx represents the voxel size. The pore volume of the micro-link, V_m, is determined by multiplying the micro-link porosity by the total volume:

$$V_m = V_m^T \phi_m \tag{14}$$

The length of the micro-link, denoted as l_m, is defined as the distance between pores i and j, subtracting their respective pore inscribed radii R_i and R_j:

$$l_m = d(i, j) - R_i - R_j \tag{15}$$

where, $d(i, j)$ represents the Euclidean distance between the centers of pores i and j. The cross-sectional area of the micro-link, denoted as A_m, is determined using:

$$A_m \propto \frac{V_m^T}{l_m}, \quad \Rightarrow \quad A_m = \beta \frac{V_m^T}{l_m} \tag{16}$$

Here, β is considered as a tuning parameter, and the same β value is used for all micro-links. We will show later that A_m will be used for micro-link conductance calculations. To calculate the micro-link flow conductance, we also need the permeability of the micro-link, denoted as K_m. The permeability is found empirically: in this paper, we use the Kozeny-Carman equation [*Kozeny*, 1927; *Carman*, 1937],

$$K_m = \frac{1}{180} \frac{\phi_m^3 \cdot d_g^2}{(1 - \phi_m)^2} \tag{17}$$

where d_g is the average grain diameter which we will use as an adjustable parameter.

2.4.3.2 **Incorporating Micro-Links in Flow Simulation:** The introduction of micro-links does not alter the total number of pores in the network, ensuring that the size of the linear system of equations remains unchanged. This is a significant advantage of representing subresolution porosity as micro-links since the number of unknown pressures remains constant. We use Eqs. (9)-(11) as before but replace the throat length L_t with the length l_m from Eq. (15) and the lengths of pores i and j with their radii. Note that if both a micro-link and a macro-throat exist between pores i and j, we separately calculate two $Q_{p,ij}$ values: one for the micro-link and one for the macro-throat, and then add them together.

The micro-link hydraulic conductance to phase p is defined as follows:

$$g_{p,m}(S_w) = \frac{K_m \cdot k_{r,p}(S_w)}{\mu_p} A_m \tag{18}$$

where K_m is micro-link permeability determined from Eq. (17), $k_{r,p}(S_w)$ is the relative permeability of phase p at brine saturation S_w, A_m denotes the cross-sectional area of the micro-link,Eq. (16), and μ_p is the dynamic viscosity of phase p. For electrical conductance we use the Archie equation [*Archie*, 1942],

$$g_{p,m}(S_w) = \frac{S_w^n}{F \cdot R_w} A_m \tag{19}$$

where R_w is the brine resistivity, n is the saturation exponent, and F is the Formation factor that is the ratio of the resistivity of a rock filled with water (R_o) to the resistivity of water alone (R_w). We assume:

$$F = \frac{R_o}{R_w} = \frac{a}{\phi_m^b} \tag{20}$$

where the constant a represents the tortuosity factor, and b is the cementation exponent.

For single-phase flow simulation, we set the water saturation (S_w) to one. From this, we determine conductances and construct the system of equations for flow and electrical conductivity through the network. Solving these systems of equations provides us with the pressure and potential fields, respectively. Next, we calculate the permeability and formation factor of the pore network system. The parameters d_g and β, Eqs. (16) and (17), are tuning parameters used to match the permeability and formation factor obtained from experiments.

In two-phase flow, we must find the brine saturation at each micro-link based on the prevailing capillary pressure. This pressure is applied to all accessible resolved elements to determine the curvature of oil/water interfaces, as well as the saturation for all elements including micro-links. To do this, we use the Leverett J-function, which relates capillary pressure to water saturation in a porous medium [*Leverett*, 1941]:

$$J(S_w) = \frac{P_c(S_w)}{\sigma} \sqrt{\frac{K_m}{\phi_m}} \tag{21}$$

where J is the Leverett J-function, P_c is the prevailing capillary pressure, σ is the interfacial tension between the fluids, K_m is the micro-link permeability, and ϕ_m is the micro-link porosity, Eq. (12). By assuming an empirical model for the J-function based on saturation, we can determine saturation from the prevailing capillary pressure. For drainage, we use the a power-law model,

$$J(S_w) = J^* S_e^{-1/\lambda} \quad \Rightarrow \quad S_e = \left(\frac{J^*}{J(S_w)}\right)^{\lambda} \tag{22}$$

here, J^* corresponds to the entry pressure. If $J(S_w)$ is less than J^*, S_e is set to 1. The parameter λ represents the power-law exponent, which determines the shape of the capillary pressure-saturation relationship. The normalized saturation of the wetting phase, denoted as S_e, can be expressed as:

$$S_e = \frac{S_w - S_{wr}}{1 - S_{or} - S_{wr}} \tag{23}$$

where S_{wr} is the residual water saturation, and S_{or} is the residual oil saturation (for drainage, S_{or} is set to zero). During drainage, we increase the prevailing capillary pressure, which causes the water saturation in the system to decrease. This continues until we reach a maximum capillary pressure, each micro-link water saturation at this point is represented by S_w^{Hyst}. Since micro-links have varying permeability and porosity, each micro-link will have a different water saturation (S_w^{Hyst}) at this capillary pressure (as given by Eq. (21)).

Despite the simplicity of the power-law model, it often provides a good approximation for the capillary pressure-saturation relationship, allowing us to determine saturation for each prevailing capillary pressure in micro-links explicitly. However, its application is limited to water-wet systems. Therefore, in this context, we only use it to describe primary drainage.

Afterward, we decrease the capillary pressure gradually to proceed with water injection. For water flooding, we employ a more elaborate model that can accommodate different wettabilities and can explicitly determine the saturation for the prevailing capillary pressure [*Foroughi et al.*, 2022]. The Leverett J-function based on this capillary pressure model is as follows:

$$J(S_w) = A + B\tan(\frac{\pi}{2} - \pi S_e^C) \tag{24}$$

with fitting parameters A, B and C. Eq. (24) can be inverted to find the saturation as a function of capillary pressure:

$$S_e = \left(\frac{1}{\pi}(\frac{\pi}{2} - \tan^{-1}(\frac{J(S_w) - A}{B}))\right)^{1/C} \tag{25}$$

After calculating the normalized water saturation, we convert it to water saturation using Eq. (23). Instead of using S_{or} and S_{wr} in Eq. (23), we use S_{nr} and S_{wr}^* to compute the micro-link saturation during waterflooding at each prevailing capillary pressure. Next, we will discuss how we obtain these two values. Firstly, by applying the Land trapping model [*Land*, 1968], we can predict the residual oil saturation, denoted as S_{nr}, at the end of waterflooding for each micro-link as follows:

$$S_{nr} = \frac{1 - S_w^{Hyst}}{1 + C_L(1 - S_w^{Hyst})} \tag{26}$$

where the coefficient C_L is determined by:

$$C_L = \frac{1}{S_{or}} - \frac{1}{1 - S_{wr}} \tag{27}$$

where we define S_{or} as the maximum residual saturation. At the start of waterflooding, we require the same $J(S_w)$ as determined by both Eq. (22) and (24). To achieve this, we introduce a pseudo residual water saturation S_{wr}^* defined as follows:

$$S_{wr}^* = \frac{S_w^{Hyst} - S_e^{Hyst} + S_e^{Hyst} \cdot S_{nr}}{1 - S_e^{Hyst}} \tag{28}$$

where using waterflooding model (Eq. (25)) S_e^{Hyst} defined as:

$$S_e^{Hyst} = \Big(\frac{1}{\pi}\big(\frac{\pi}{2} - \tan^{-1}\big(\frac{J^{PD}(S_w^{Hyst}) - A}{B}\big)\big)\Big)^{1/C} \tag{29}$$

Now that we have determined S_{nr} and S^*_{wr}, we use these values instead of S_{or} and S_{wr} in Eq. (23) to compute the micro-link saturation during waterflooding at each prevailing capillary pressure.

To examine the behavior of the Leverett J-function for both drainage and waterflooding, refer to the results illustrated in Figure 6a. The Leverett J-function for primary drainage is determined using Eq. (22), while for waterflooding, it is found using Eq. (24).

After calculating the micro-link saturations, we can predict the micro-link flow and electrical conductances using Eqs. (18) and (19), respectively. For flow conductance, empirical models for the relative permeabilities of micro-links are required. As mentioned earlier, we adopt power-law models to describe the relative permeabilities of micro-links. These expressions are often referred to as modified Brooks-Corey relations [*Brooks and Corey*, 1964],

$$k_{rw}(S_w) = k_{rw}^{max} S_e^{\alpha_w} \tag{30}$$

$$k_{ro}(S_w) = k_{ro}^{max}(1 - S_e)^{\alpha_o} \tag{31}$$

where k_{rw}^{max} and k_{ro}^{max} represent the endpoint relative permeabilities for water and oil, respectively. α_w and α_o are power law exponents. To account for hysteresis, we employ the Killough model [*Killough*, 1976]. For illustrative purposes, the relative water and oil permeabilities for various S_w^{Hyst} values are depicted in Figures 6b and 6c.

2.4.3.3 **Bypassing Zero Saturation in Two-phase Conductivity:** In our study of two-phase flow, we encountered a situation where the saturation of the wetting phase in a pore became very low, effectively halting the flow (see Figure 7). To handle this situation and to ensure continuity of flow when water is present in micro-links, we devised a bypassing mechanism. This mechanism works by rerouting the flow around the pore with zero or very low saturation for the wetting phase, allowing the flow to continue despite the blockage. To facilitate this bypassing mechanism, we set $L_{ij}/g_{p,ij}$ to $L_m/g_{p,ij}$ whenever $L_{ij}/g_{p,ij}$, calculated using Eq. (11), is less than $L_m/g_{p,ij}$. This adjustment allows us to maintain a non-zero conductance.

In the following section, we will evaluate the performance of the multiscale pore network model using the aforementioned Estaillades rock sample as a benchmark.

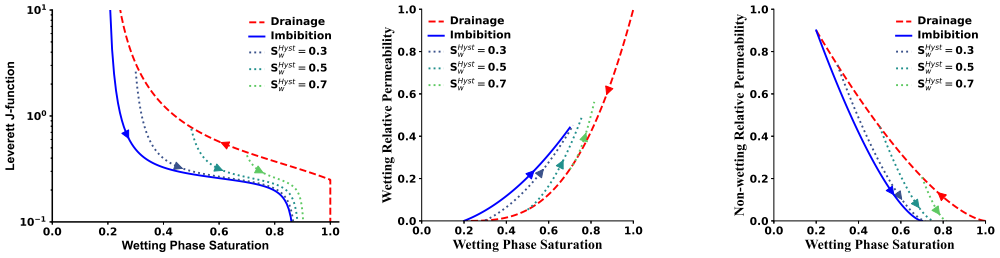

(a) (b) (c)

Figure 6. (a) Illustrates the behavior of the Leverett J-function employed in our model. The diagram depicts the power-law model for drainage, Eq. (22), and our proposed model, Eq. (24), for waterflooding. We present the results for three different saturations based on our proposed model, Eq. (24), considering potential variations in saturation following primary drainage. (b) This graph shows the water relative permeability using the Killough hysteresis model based on power-law relative permeability (k_{rw}) during drainage and waterflooding. (c) This graph shows the oil relative permeability using the Killough hysteresis model based on power-law relative permeability (k_{rnw}) during waterflooding. The model considers three initial saturations at the start of waterflooding, denoted as S_w^{Hyst}.

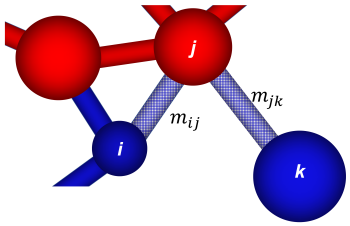

Figure 7. Illustration of a pore, denoted as j, located between two micro-links (m_{ij} and m_{jk}), while all other elements belong to resolved porosity. This pore tends to fill before the micro-links (with blue representing the wetting phase and red representing the non-wetting phase), requiring a bypass of pore j to ensure that the flow is directed exclusively through the micro-links, thereby avoiding fluid trapping.

3 Results and Discussion

In this section, we will evaluate the performance of our multiscale pore network model. The benchmark for this assessment is the Estaillades rock sample, described in Section 2.3.

Estaillades rock is a heterogeneous material characterized by a broad range of pore throat sizes. Figure 8 depicts the throat size distribution obtained from MICP porosimetry, as reported by *Tanino*

595 *and Blunt* [2012]. This distribution spans from a few nanometers to tens of micrometers, indicating
596 a wide range of radii.

597 We use the voxel size as a threshold (red dashed line in Figure 8) to distinguish between resolved
598 and unresolved pore space noting that more than one voxel is required to accurately resolve the width
599 of a pore or throat. For heterogeneous rocks such as Estaillades, the throat size distribution typically
600 exhibits a bimodal pattern: the peak at smaller radii corresponds to micro-pores and micro-throats,
601 while the peak at larger radii represents macro-pores and macro-throats. By scrutinizing the voxel
602 size threshold and the distribution, we can differentiate between two types of unresolved pore space:
603 micro-pores associated with the first peak, and macro-pores linked to the second.

607 Considering the considerable fraction of unresolved macro-pores (see Figure 8), our multiscale
modeling approach needs to accurately differentiate them from micro-pores.

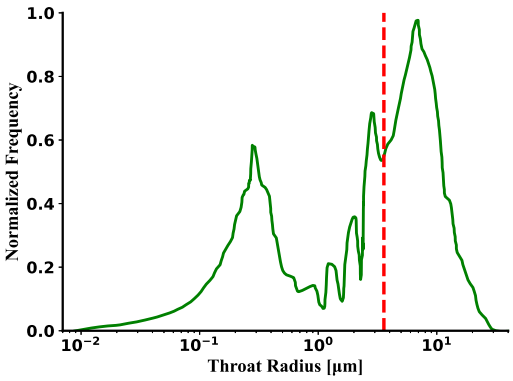

604 **Figure 8.** The throat radius distribution for the Estaillades Limestone is depicted here, highlighting the clear
605 presence of a bimodal pore size distribution. The dashed line represents the image voxel size of 3.58 μm. Data
606 from *Tanino and Blunt* [2012].

608

609 The subsequent sections present single-phase flow results based on this multiscale pore network.
610 Here, we tune the parameters of the micro-links to match the experimental permeability. Next, we
611 focus on two-phase flow simulations. Initially, we match the reported primary drainage capillary
612 pressure for Estaillades. Following this, we present the drainage relative permeability results. In the
613 end, we display the predicted results for waterflooding relative permeability, comparing them against
614 the experimentally measured values.

615 The equations to be used in the following sections are summarized in Table 1.

Table 1. Summary of parameters and equations used for micro-links.

Parameter	Model
Residual water saturation	$S_{wi} = 0.1$
Residual oil saturation	$S_{or} = 0.1$
Archie model for conductivity Eq. (19)	$\sigma_m^E = \frac{S_w^2 \phi^{1.9}}{R_w}$
Assumed analytical relation for J in primary drainage Eq. (22)	$J(S_w) = 0.25 S_e^{-1}$
Assumed analytical relation for J in waterflooding Eq. (24)	$J(S_w) = 0.2 + 0.01 \tan\left(\frac{\pi}{2} - \pi S_e^{1.5}\right)$
Corey model for water relative permeability in drainage Eq. (30)	$k_{rw} = S_e^4$
Corey model for oil relative permeability in drainage Eq. (31)	$k_{ro} = 0.9(1 - S_e)^2$
Corey model for water relative permeability in waterflooding Eq. (30)	$k_{rw} = 0.5 S_e^4$
Corey model for oil relative permeability in waterflooding Eq. (31)	$k_{ro} = 0.6(1 - S_e)^2$

3.1 Single-Phase Flow - Model Tuning

In this section, we present the results of single-phase flow analysis conducted on three sub-volumes of the sample. Each sub-volume consists of $1127 \times 1127 \times 1127$ voxels, representing a substantial portion of the rock sample. The analysis focused on determining the permeability and formation factor, which were obtained through simulations. Permeability was calculated using Eq. (7) through the simulation of flow within the extracted pore network. The formation factor was determined by simulating the electrical current through the rock and calculating its electrical resistivity (the inverse of electrical conductivity). Eq. (20) was then employed to calculate the formation factor.

For single-phase fluid flow simulations, we use the Carman-Kozeny equation (See Eq. (18)) to calculate the conductance of micro-links. Two distinct grain diameters (d_g) have been used: 14.0 μm and 1.75 μm. This choice is essential to account for the capillary pressure behavior seen in the MICP tests. We will explain the implementation technique in more detail later in the paper. By using two different grain diameters, we can account for two types of unresolved porosity. The selection of these two values allows us to tune the capillary behavior observed in the MICP tests during drainage, while also aligning with the experimental permeability at the same time. For electrical simulations, we use an empirical conductivity model for micro-links based on Archie's law (see Table 1 for the exact form).

The results for single-phase flow are presented in Table 2. To assess the influence of sub-resolution porosity on flow behavior, two simulation types were compared. The first simulation disregarded the presence of sub-resolution porosity, while the second simulation, based on our methodology, considered the micro-porous nature of the rock. By comparing these two simulations, we can evaluate the impact of sub-resolution porosity on flow characteristics within the sub-volumes.

Additionally, as shown in Table 2, we have reported the corresponding porosity values for each sub-volume. The analysis revealed that all three sub-volumes exhibited similar fractions of resolved and unresolved pore space. When sub-resolution porosity was not considered, the predicted permeability using pore network modeling was consistently one order of magnitude lower than the experimentally measured permeability. Similarly, the predicted formation factors exhibited unreasonably high values (see Table 2).

However, by incorporating sub-resolution porosity and implementing our multiscale pore network model, we successfully calibrated the micro-link parameter to obtain reasonable permeability values that aligned with the experimental measurements (see Table 2 for all sub-volumes). Furthermore, the predicted formation factors experienced a significant improvement and fell within the reported range for carbonate rocks, namely 10-100 [*Youssef et al.*, 2008].

It is worth noting that the tuning parameters in this study included the constant d_g, which corresponds to the grain diameter in the Kozeny-Carman relation, and the parameter β which scales the micro-link cross-sectional area in Eq. (16). By carefully adjusting these parameters, we managed to achieve more accurate simulations that closely aligned with experimental values for permeability and formation factor. In this context, a calibrated value of 2.5 was used for β across all sub-volumes. The tuned value for d_g will be discussed in the next section.

Table 2. Comparison of experimental and sub-volume data.

	ϕ [%]	k [mD]	F
Experimental	28.2 ± 1.5	128 ± 4	n/a
Sub-volume 1 (resolved pore space)	9.8	12	1064
Sub-volume 1 (multiscale)	29.7	130	53
Sub-volume 2 (resolved pore space)	9.1	10	2153
Sub-volume 2 (multiscale)	28.7	132	59
Sub-volume 3 (resolved pore space)	10.2	27	711
Sub-volume 3 (multiscale)	30.2	162	51

3.2 Two-Phase Flow - Model Tuning

In this section we tune our model to mimic reported MICP for Estaillades in the literature. As mentioned earlier, the throat size distribution from the MICP tests for Estaillades rock displays two distinct peaks, corresponding to two types of porosity. Additionally, based on Figure 8 and considering the measured voxel size of the sample (3.58 μm), it is evident that a significant fraction of the pore space in this rock remains unresolved. We assign the grain diameter to each micro-link as follows:

$$\phi_{m,c} = \mathcal{N}(\overline{\phi_m}, 0.25\sigma^2_{\phi_m}) \quad \Rightarrow \quad d_g = \begin{cases} 14.0\,\mu m, & \text{if } \phi_m > \phi_{m,c} \\ 1.75\,\mu m, & \text{if } \phi_m <= \phi_{m,c} \end{cases} \tag{32}$$

Here, $\overline{\phi_m}$ represents the mean porosity of micro-links, and σ_{ϕ_m} is the standard deviation of micro-link porosity. Additionally, $\phi_{m,c}$ denotes the porosity criterion value corresponding to each micro-link, which is used to assign d_g to that micro-link.

The $\mathcal{N}$ symbol represents a random selection of $\phi_{m,c}$ from a normal distribution with the mean and standard deviation indicated. Then the d_g and hence permeability, Eq. (17), of the micro-link is then determined based on the thresholds shown in Eq. (32). This probabilistic model allows the capillary pressure to vary smoothly in the transition from resolved macro-pores, to unresolved but larger pores to true micro-porosity, to reproduce the behavior observed in Figure 9.

It is assumed that the pores and throats extracted from the resolved pore space are strongly water-wet, with a contact angle of 0° for drainage. The Leverett J-function used for primary drainage is presented in Table 1.

To validate the performance of our approach, we generated capillary pressure for three sub-volumes of the Estaillades rock sample (Figure 9). We then compared these results with experimental MICP data from two literature sources: *Tanino and Blunt* [2012] and *Alyafei and Blunt* [2016]. There is excellent agreement between the simulated and experimental results. The simulated capillary pressure values were slightly higher than the data of *Alyafei and Blunt* [2016], which may be due to the lower permeability observed in our sample which is not fully accounted for by J-function scaling. *Alyafei and Blunt* [2016] reported a permeability of 182 mD, while the sample studied by *Tanino and Blunt* [2012] had a permeability of 166 mD compared to our value of 128 mD. Note that hereafter we have used the colors orange, purple, and teal to indicate the results of sub-volumes 1, 2, and 3, respectively.

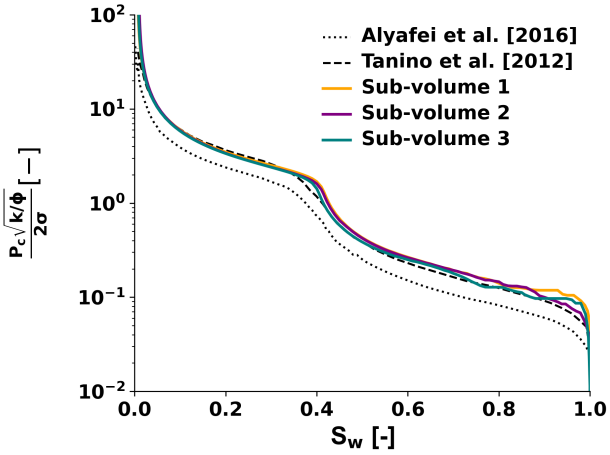

Figure 9. Dimensionless measured capillary pressure (written as a dimensionless J function, Eq. (21)) as a function of water saturation and the results of multiscale modeling for three different sub-volumes. Data from *Tanino and Blunt* [2012] and *Alyafei and Blunt* [2016].

3.3 Prediction and Validation

In Figure 10, we depict the primary drainage relative permeability for three distinct sub-volumes of the Estaillades sample. The graphs in Figures 10a and 10b show the same data on Cartesian and

logarithmic y-axes respectively. The relative permeability trends of water and oil are generally similar across all sub-volumes. Here, however, we do not have experimental data for comparison.

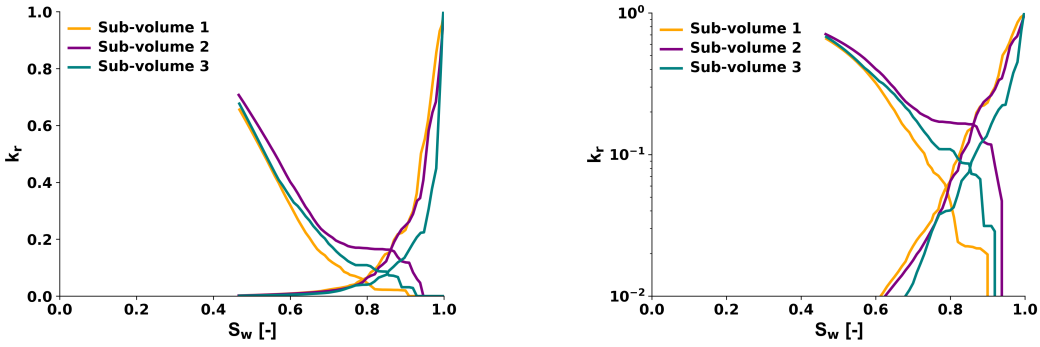

Figure 10. Comparative analysis of relative permeability for water and oil across three distinct Estaillades sub-volumes, obtained during the drainage with our multiscale pore network model.

The final results of relative permeability for waterflooding in the Estaillades sample are plotted against experimentally determined values in Figure 11. For the sake of clarity, we have presented each subvolume using separate plots. The various lines on the graph represent the inherent uncertainties associated with pore network modeling and different assumptions about initial saturation. For each subvolume, we generated 310 realizations by varying the initial brine saturation and using different seeds for the waterflooding simulations. The initial brine saturation is consistent and within the range of the experiments. The results are shown on both Cartesian (Figures 11a, 11c, and 11e) and logarithmic scales (Figures 11b, 11d, and 11f), and fall within the bounds of experimental uncertainty.

The relative permeability model for micro-links (Table 1) assumes water-wet behavior during waterflooding. Pores and throats extracted from the resolved pore space are considered water-wet, with a contact angle of 45° for waterflooding. This contact angle is similar to the one reported for the water-wet Bentheimer sample in our previous studies [*Blunt et al.*, 2019]. The selection of the capillary pressure empirical model and the relative permeability empirical models of the micro-link significantly influence these results. In this study, the capillary pressure model, as depicted in Figure 6a, exhibits typical water-wet behavior.

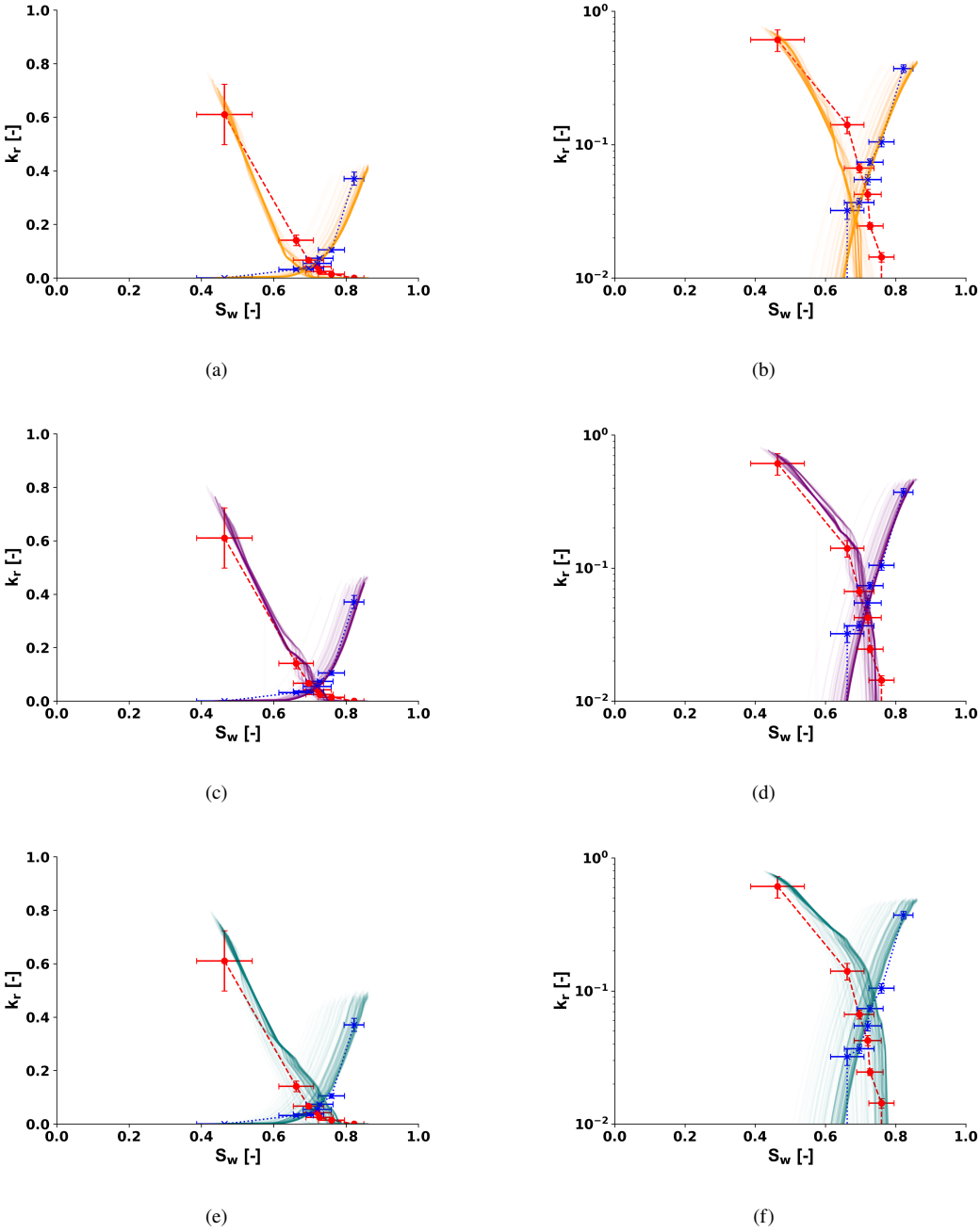

Figure 11. Comparative analysis of relative permeability for water and oil for three Estaillades sub-volumes, obtained during waterflooding using our multiscale pore network model, versus experimental results. A good agreement between the modeling and experimental data is evident. The error bars represent the uncertainty in the experimental measurements, determined by taking into account the uncertainties in the input parameters and the uncertainty ranges evaluated by including the saturation profile in addition to experimental uncertainty (see [*Zhang et al.*, 2023b] for further details). The blue dotted line corresponds to the experimental relative permeability of water, and the red dashed line corresponds to the experimental relative permeability of oil. Figures (a) and (b) correspond to sub-volume 1, Figures (c) and (d) correspond to sub-volume 2, and Figures (e) and (f) correspond to sub-volume 3. These modeling results are derived from 310 realizations.

The choice of empirical models to describe flow in micro-links is critical and a preliminary understanding of the relationship between wettability and sub-resolution pore structure is necessary. Experimental parameters such as permeability, formation factor, and MICP can provide valuable insights into these uncertain aspects. Additionally, a general understanding of wettability is beneficial in assigning the correct empirical model for micro-links.

This approach can aid in characterizing and understanding both single and two-phase flow through all types of porous materials with wide pore size distributions.

4 Conclusions and future work

In this study, we present a novel workflow to develop a multiscale pore network model capable of simulating fluid flow in heterogeneous rocks with unresolved porosity. The model incorporates Darcy-type elements known as micro-links, enabling accurate representation of the pore space and flow behavior. Incorporation of this unresolved pore space in modeling is crucial for obtaining accurate pore volume measurements and ensuring correct accessibility and flow.

We treat sub-resolution porosity as micro-links that connect the nearest resolved pores found using dilation-based algorithm. This algorithm assigns each grain voxel, which contains sub-resolution porosity, to its two closest resolved pores. Voxel groups with the same two nearest pores are categorized as a micro-link connecting them. We employ empirical models to calculate capillary pressure and relative permeability through the micro-links.

We test our model on Estaillades carbonate which has a wide range of pore size. We use differential imaging to identify both the resolved macro-pore space and unresolved porosity. We first tune the model parameters to provide a good match to the measured permeability and drainage capillary pressure. We assign two types of micro-links based on their porosity: the more porous links are assumed to be principally associated with pores whose size is just below the image resolution, while lower porosity elements represent smaller micro-porosity.

We predict both drainage and waterflooding relative permeabilities for water-wet conditions. The predicted waterflood relative permeabilities fall within the uncertainty of the experimental measurements.

In the future, our intention is to expand the application of this methodology, coupled with our wettability optimization workflow [*Foroughi et al.*, 2020, 2021], across a diverse range of datasets.

Open Research

he source code for this project is available on Zenodo [*Foroughi et al.*, 2023] and in this GitHub repository: https://github.com/ImperialCollegeLondon/porescale. The repository contains all the codes used in this paper. The image data used in this work can be found on Figshare [*Gao et al.*, 2023].

Acknowledgments

This work was funded under the Shell Digital Rocks Programme also part of the EPSRC INFUSE prosperity partnership, grant number EP/V038044/1. We thank S. Berg from Shell for his helpful and insightful comments on this work.

5 Appendix

5.1 Experimental Procedure

The experimental procedure was akin to other studies on intermittency by *Gao et al.* [2019], consisting of the following steps:

1. The flow cell was subjected to a confining pressure of 2 MPa to compress the Viton sleeve around the rock sample, preventing fluid bypass. Two dry (air) scans were performed on the upper and lower sections of the sample over an 80-minute period at ambient conditions. The overlap between the scans was approximately 25%, facilitating the stitching of the two scans post-reconstruction.
2. CO_2 was injected into the rock sample for over 30 min to displace the air.
3. Injection of brine followed, achieving complete saturation of the sample. A differential pressure transducer (PD-33X, Keller) was positioned along the tubing.
4. The sample was flushed with over 1000 pore volumes of brine at 1 mL/min to ensure the rock was completely filled with brine.
5. Two brine scans, similar to the dry scans, were captured over 80 min. A back pressure of 2000 kPa was set for the entire system and the confining pressure was adjusted to 4 MPa.
6. Primary drainage ensued with the injection of oil at a high flow rate of 2 mL/min for 30 min. This allowed us to achieve a uniform initial brine saturation along the sample.
7. The injection of oil continued at a flow rate of 0.02 mL/min, while the brine fractional flow was set to 0. Injection proceeded until a steady state was reached, identifiable by a constant pressure drop sustained for over 2 hours. In our experiment, approximately 24 hours was required to attain this state. Subsequently, scans were taken at the same position of the core over an 80-minute period without interruption of the flow.
8. Step 7 replicated for fractional flows, f_w, of 0.15, 0.3, 0.5, 0.7, and 0.85. The total volumetric flow rate remained fixed as the oil flow rate decreased from 0.017 mL/min to 0.003 mL/min and the brine flow rate increased from 0.003 mL/min to 0.017 mL/min. This entire process represented an imbibition displacement in this water-wet sample (brine as the wetting phase). Concurrently, the pressure drop across the entire sample was recorded. Reaching a steady state for each fractional flow experiment took approximately 16–25 hours. Two scans were performed at the same position of the core over an 80-minute period without halting the flow.

9. Brine was injected at a low flow rate (0.02 mL/min) for 30 min to achieve the residual oil saturation. Then, brine injection continued at 0.02 mL/min to measure the steady-state pressure difference at a fractional flow of 1.
10. Following a thorough cleaning of all the tubing and end fittings used in the experiment, steps 7 to 9 were applied to the entire system excluding the rock sample. The pressure drops of the tubing itself were recorded at all fractional flows, ranging from 2 kPa to 20 kPa. The minimum pressure drop was obtained when f_w was 0, while the maximum was achieved when f_w was 0.85.
11. The pressure differences along the cores were computed by subtracting the pressure drops along the tubing (measured in step 10) from the total pressure drops (measured from steps 7 to 9).

References

Akai, T., A. M. Alhammadi, M. J. Blunt, and B. Bijeljic (2019), Modeling oil recovery in mixed-wet rocks: pore-scale comparison between experiment and simulation, *Transport in Porous Media*, *127*(2), 393–414.

Alyafei, N., and M. J. Blunt (2016), The effect of wettability on capillary trapping in carbonates, *Advances in Water Resources*, *90*, 36–50.

Andreas, J., E. Hauser, and W. Tucker (2002), Boundary tension by pendant drops1, *The Journal of Physical Chemistry*, *42*(8), 1001–1019.

Archie, G. E. (1942), The electrical resistivity log as an aid in determining some reservoir characteristics, *Transactions of the AIME*, *146*(01), 54–62.

Armstrong, R. T., J. E. McClure, V. Robins, Z. Liu, C. H. Arns, S. Schlüter, and S. Berg (2019), Porous media characterization using minkowski functionals: Theories, applications and future directions, *Transport in Porous Media*, *130*, 305–335.

Bauer, D., S. Youssef, M. Han, S. Bekri, E. Rosenberg, M. Fleury, and O. Vizika (2011), From computed microtomography images to resistivity index calculations of heterogeneous carbonates using a dual-porosity pore-network approach: Influence of percolation on the electrical transport properties, *Physical review E*, *84*(1), 011,133.

Bauer, D., S. Youssef, M. Fleury, S. Bekri, E. Rosenberg, and O. Vizika (2012), Improving the estimations of petrophysical transport behavior of carbonate rocks using a dual pore network approach combined with computed microtomography, *Transport in porous media*, *94*, 505–524.

Bear, J., and A. H.-D. Cheng (2010), *Modeling groundwater flow and contaminant transport*, vol. 23, Springer.

Bekri, S., C. Laroche, and O. Vizika (2005), Pore network models to calculate transport and electrical properties of single or dual-porosity rocks, in *SCA*, vol. 35, p. 2005.

Bijeljic, B., P. Mostaghimi, and M. J. Blunt (2013), Insights into non-fickian solute transport in carbonates, *Water resources research*, *49*(5), 2714–2728.

Bijeljic, B., A. Q. Raeini, Q. Lin, and M. J. Blunt (2018), Multimodal functions as flow signatures in complex porous media, *arXiv preprint arXiv:1807.07611*.

Blunt, M. J. (2001), Flow in porous media—pore-network models and multiphase flow, *Current opinion in colloid & interface science*, *6*(3), 197–207.

Blunt, M. J. (2017), *Multiphase flow in permeable media: A pore-scale perspective*, Cambridge University Press.

Blunt, M. J. (2022), Ostwald ripening and gravitational equilibrium: Implications for long-term subsurface gas storage, *Physical Review E*, *106*(4), 045,103.

Blunt, M. J., M. D. Jackson, M. Piri, and P. H. Valvatne (2002), Detailed physics, predictive capabilities and macroscopic consequences for pore-network models of multiphase flow, *Advances in Water Resources*, *25*(8-12), 1069–1089.

Blunt, M. J., B. Bijeljic, H. Dong, O. Gharbi, S. Iglauer, P. Mostaghimi, A. Paluszny, and C. Pentland (2013), Pore-scale imaging and modelling, *Advances in Water Resources*, *51*, 197–216.

Blunt, M. J., Q. Lin, T. Akai, and B. Bijeljic (2019), A thermodynamically consistent characterization of wettability in porous media using high-resolution imaging, *Journal of Colloid and Interface Science*, *552*, 59–65.

Boot-Handford, M. E., J. C. Abanades, E. J. Anthony, M. J. Blunt, S. Brandani, N. Mac Dowell, J. R. Fernández, M.-C. Ferrari, R. Gross, J. P. Hallett, et al. (2014), Carbon capture and storage update, *Energy & Environmental Science*, *7*(1), 130–189.

Brinkman, H. C. (1949), A calculation of the viscous force exerted by a flowing fluid on a dense swarm of particles, *Flow, Turbulence and Combustion*, *1*, 27–34.

Brooks, R., and A. Corey (1964), Hydraulic properties of porous media. hydrology paper no. 3, *Civil Engineering Department, Colorado State University, Fort Collins, CO*.

Buades, A., B. Coll, and J.-M. Morel (2005), A non-local algorithm for image denoising, in *2005 IEEE computer society conference on computer vision and pattern recognition (CVPR'05)*, vol. 2, pp. 60–65, Ieee.

Buades, A., B. Coll, and J.-M. Morel (2008), Nonlocal image and movie denoising, *International journal of computer vision*, *76*, 123–139.

Bultreys, T., L. Van Hoorebeke, and V. Cnudde (2015), Multi-scale, micro-computed tomography-based pore network models to simulate drainage in heterogeneous rocks, *Advances in Water Resources*, *78*, 36–49.

Bultreys, T., L. Van Hoorebeke, and V. Cnudde (2016), Simulating secondary waterflooding in heterogeneous rocks with variable wettability using an image-based, multiscale pore network model, *Water Resources Research*, *52*(9), 6833–6850.

Bultreys, T., Q. Lin, Y. Gao, A. Q. Raeini, A. AlRatrout, B. Bijeljic, and M. J. Blunt (2018), Validation of model predictions of pore-scale fluid distributions during two-phase flow, *Physical Review E*, *97*(5), 053,104.

Burger, W., and M. J. Burge (2022), *Digital Image Processing: An Algorithmic Introduction*, Springer Nature.

Carman, P. C. (1937), Fluid flow through a granular bed, *Trans. Inst. Chem. Eng. London*, *15*, 150–156.

Carrillo, F. J., and I. C. Bourg (2019), A darcy-brinkman-biot approach to modeling the hydrology and mechanics of porous media containing macropores and deformable microporous regions, *Water Resources Research*, *55*(10), 8096–8121.

Da Wang, Y., M. J. Blunt, R. T. Armstrong, and P. Mostaghimi (2021), Deep learning in pore scale imaging and modeling, *Earth-Science Reviews*, *215*, 103,555.

Dinariev, O., N. Evseev, and D. Klemin (2020), Density functional hydrodynamics in multiscale pore systems: Chemical potential drive, in *E3S Web of Conferences*, vol. 146, p. 01001, EDP Sciences.

Dong, H., and M. J. Blunt (2009), Pore-network extraction from micro-computerized-tomography images, *Physical review E*, *80*(3), 036,307.

Foroughi, S., S. Jamshidi, and M. R. Pishvaie (2018), New correlative models to improve prediction of fracture permeability and inertial resistance coefficient, *Transport in Porous Media*, *121*, 557–584.

Foroughi, S., B. Bijeljic, Q. Lin, A. Q. Raeini, and M. J. Blunt (2020), Pore-by-pore modeling, analysis, and prediction of two-phase flow in mixed-wet rocks, *Physical Review E*, *102*(2), 023,302.

Foroughi, S., B. Bijeljic, and M. J. Blunt (2021), Pore-by-pore modelling, validation and prediction of waterflooding in oil-wet rocks using dynamic synchrotron data, *Transport in Porous Media*, *138*(2), 285–308.

Foroughi, S., B. Bijeljic, and M. J. Blunt (2022), A closed-form equation for capillary pressure in porous media for all wettabilities, *Transport in Porous Media*, *145*(3), 683–696.

Foroughi, S., A. Q. Raeini, B. Bijeljic, and M. J. Blunt (2023), Pore scale modeling codes, doi: 10.5281/zenodo.8411328.

Gao, Y., A. Q. Raeini, M. J. Blunt, and B. Bijeljic (2019), Pore occupancy, relative permeability and flow intermittency measurements using x-ray micro-tomography in a complex carbonate, *Advances in Water Resources*, *129*, 56–69.

Gao, Y., S. FOROUGHI, B. Bijeljic, and M. J. Blunt (2023), estaillades carbonate: High-resolution x-ray imaging of steady-state oil-brine flow in microporous rock, doi:10.6084/M9.FIGSHARE.24261109.

Giudici, L. M., A. Q. Raeini, M. J. Blunt, and B. Bijeljic (2023), Representation of fully three-dimensional interfacial curvature in pore-network models, *Water Resources Research*, p. e2022WR033983.

Guo, B., L. Ma, and H. A. Tchelepi (2018), Image-based micro-continuum model for gas flow in organic-rich shale rock, *Advances in Water Resources*, *122*, 70–84.

Jiang, Z., M. Van Dijke, K. S. Sorbie, and G. D. Couples (2013), Representation of multiscale heterogeneity via multiscale pore networks, *Water resources research*, *49*(9), 5437–5449.

Joekar-Niasar, V., M. Prodanović, D. Wildenschild, and S. Hassanizadeh (2010), Network model investigation of interfacial area, capillary pressure and saturation relationships in granular porous media, *Water Resources Research*, *46*(6).

Juanes, R., E. Spiteri, F. Orr Jr, and M. Blunt (2006), Impact of relative permeability hysteresis on geological CO_2 storage, *Water resources research*, *42*(12).

Killough, J. (1976), Reservoir simulation with history-dependent saturation functions, *Society of Petroleum Engineers Journal*, *16*(01), 37–48.

Kozeny, J. (1927), Ueber kapillare leitung des wassers im boden, *Sitzungsberichte der Akademie der Wissenschaften in Wien*, *136*, 271.

Land, C. S. (1968), Calculation of imbibition relative permeability for two-and three-phase flow from rock properties, *Society of Petroleum Engineers Journal*, *8*(02), 149–156.

Lesinigo, M., C. D'Angelo, and A. Quarteroni (2011), A multiscale darcy–brinkman model for fluid flow in fractured porous media, *Numerische Mathematik*, *117*, 717–752.

Leu, L., S. Berg, F. Enzmann, R. T. Armstrong, and M. Kersten (2014), Fast x-ray micro-tomography of multiphase flow in berea sandstone: A sensitivity study on image processing, *Transport in Porous Media*, *105*(2), 451–469.

Leverett, M. (1941), Capillary behavior in porous solids, *Transactions of the AIME*, *142*(01), 152–169.

Li, M., S. Foroughi, J. Zhao, B. Bijeljic, and M. J. Blunt (2023), Image-based pore-scale modelling of the effect of wettability on breakthrough capillary pressure in gas diffusion layers, *Journal of Power Sources*, *584*, 233,539.

Lin, Q., Y. Al-Khulaifi, M. J. Blunt, and B. Bijeljic (2016), Quantification of sub-resolution porosity in carbonate rocks by applying high-salinity contrast brine using x-ray microtomography differential imaging, *Advances in water resources*, *96*, 306–322.

Lin, Q., B. Bijeljic, S. Foroughi, S. Berg, and M. J. Blunt (2021), Pore-scale imaging of displacement patterns in an altered-wettability carbonate, *Chemical Engineering Science*, *235*, 116,464.

McClure, J. E., R. T. Armstrong, M. A. Berrill, S. Schlüter, S. Berg, W. G. Gray, and C. T. Miller (2018), Geometric state function for two-fluid flow in porous media, *Physical Review Fluids*, *3*(8), 084,306.

Meakin, P., and A. M. Tartakovsky (2009), Modeling and simulation of pore-scale multiphase fluid flow and reactive transport in fractured and porous media, *Reviews of Geophysics*, *47*(3), RG3002.

Mehmani, A., and M. Prodanović (2014), The effect of microporosity on transport properties in porous media, *Advances in Water Resources*, *63*, 104–119.

Mehmani, A., M. Prodanović, and F. Javadpour (2013), Multiscale, multiphysics network modeling of shale matrix gas flows, *Transport in porous media*, *99*(2), 377–390.

Moghadasi, R., S. Foroughi, F. Basirat, S. McDougall, A. Tatomir, B. Bijeljic, M. J. Blunt, and A. Niemi (2023), Pore-scale determination of residual gas remobilization and critical saturation in geological CO_2 storage: A pore-network modelling approach, *Water Resources Research*, p. e2022WR033686.

Mostaghimi, P., M. J. Blunt, and B. Bijeljic (2013), Computations of absolute permeability on micro-ct images, *Mathematical Geosciences*, *45*, 103–125.

Øren, P., L. Ruspini, M. Saadatfar, R. Sok, M. Knackstedt, and A. Herring (2019), In-situ pore-scale imaging and image-based modelling of capillary trapping for geological storage of CO_2, *International Journal of Greenhouse Gas Control*, *87*, 34–43.

Oren, P. E., L. Ruspini, M. Saadatfar, A. Herring, R. Sok, and M. Knackstedt (2018), In-situ pore-scale imaging and image-based modelling of capillary trapping for geological storage of supercritical CO_2, in *14th Greenhouse Gas Control Technologies Conference Melbourne*, pp. 21–26.

Ott, H., C. Pentland, and S. Oedai (2015), CO_2–brine displacement in heterogeneous carbonates, *International Journal of Greenhouse Gas Control*, *33*, 135–144.

Prodanović, M., A. Mehmani, and A. P. Sheppard (2015), Imaged-based multiscale network modelling of microporosity in carbonates, *Geological Society, London, Special Publications*, *406*(1), 95–113.

Raeini, A. Q., M. J. Blunt, and B. Bijeljic (2012), Modelling two-phase flow in porous media at the pore scale using the volume-of-fluid method, *Journal of Computational Physics*, *231*(17), 5653–5668.

Raeini, A. Q., M. J. Blunt, and B. Bijeljic (2014), Direct simulations of two-phase flow on micro-ct images of porous media and upscaling of pore-scale forces, *Advances in water resources*, *74*, 116–126.

Raeini, A. Q., B. Bijeljic, and M. J. Blunt (2017), Generalized network modeling: Network extraction as a coarse-scale discretization of the void space of porous media, *Physical Review E*, *96*(1), 013,312.

Raeini, A. Q., B. Bijeljic, and M. J. Blunt (2018), Generalized network modeling of capillary-dominated two-phase flow, *Physical Review E*, *97*(2), 023,308.

963 Raeini, A. Q., J. Yang, I. Bondino, T. Bultreys, M. J. Blunt, and B. Bijeljic (2019), Validating the
964 generalized pore network model using micro-ct images of two-phase flow, *Transport in Porous*
965 *Media*, *130*(2), 405–424.
966 Ruspini, L., P. Øren, S. Berg, S. Masalmeh, T. Bultreys, C. Taberner, T. Sorop, F. Marcelis, M. Appel,
967 J. Freeman, et al. (2021), Multiscale digital rock analysis for complex rocks, *Transport in Porous*
968 *Media*, *139*(2), 301–325.
969 Sahimi, M. (2011), *Flow and transport in porous media and fractured rock: from classical methods*
970 *to modern approaches*, John Wiley & Sons.
971 Saxena, N., R. Hofmann, F. O. Alpak, J. Dietderich, S. Hunter, and R. J. Day-Stirrat (2017), Effect
972 of image segmentation & voxel size on micro-ct computed effective transport & elastic properties,
973 *Marine and Petroleum Geology*, *86*, 972–990.
974 Saxena, N., A. Hows, R. Hofmann, F. O. Alpak, J. Dietderich, M. Appel, J. Freeman, and H. De Jong
975 (2019), Rock properties from micro-ct images: Digital rock transforms for resolution, pore volume,
976 and field of view, *Advances in Water Resources*, *134*, 103,419.
977 Shokri-Kuehni, S. M., M. N. Rad, C. Webb, and N. Shokri (2017), Impact of type of salt and ambient
978 conditions on saline water evaporation from porous media, *Advances in water resources*, *105*,
979 154–161.
980 Stauffer, C. E. (1965), The measurement of surface tension by the pendant drop technique, *The*
981 *journal of physical chemistry*, *69*(6), 1933–1938.
982 Tanino, Y., and M. J. Blunt (2012), Capillary trapping in sandstones and carbonates: Dependence
983 on pore structure, *Water Resources Research*, *48*(8).
984 Valvatne, P. H., and M. J. Blunt (2004), Predictive pore-scale modeling of two-phase flow in mixed
985 wet media, *Water Resources Research*, *40*(7), W07,406.
986 Wang, S., A. Mascini, L. C. Ruspini, P. E. Oren, and T. Bultreys (2022), Imaging and modelling the
987 impact of multi-scale pore connectivity on two-phase flow in mixed-wet rock, *Authorea Preprints*.
988 Wu, Y., P. Tahmasebi, K. Liu, S. Fagbemi, C. Lin, S. An, and L. Ren (2022), Two-phase flow in
989 heterogeneous porous media: A multiscale digital model approach, *International Journal of Heat*
990 *and Mass Transfer*, *194*, 123,080.
991 Youssef, S., M. Han, D. Bauer, E. Rosenberg, S. Bekri, M. Fleury, and O. Vizika (2008), High
992 resolution μ-ct combined to numerical models to assess electrical properties of bimodal carbonates,
993 in *International symposium of core analysts*, pp. 1–12.
994 Zhang, G., S. Foroughi, A. Q. Raeini, M. J. Blunt, and B. Bijeljic (2023a), The impact of bimodal pore
995 size distribution and wettability on relative permeability and capillary pressure in a microporous

limestone with uncertainty quantification, *Advances in Water Resources*, *171*, 104,352.

Zhang, G., S. Foroughi, B. Bijeljic, and M. J. Blunt (2023b), A method to correct steady-state relative permeability measurements for inhomogeneous saturation profiles in one-dimensional flow, *Transport in Porous Media*, pp. 1–16.

Zhang, Y., B. Bijeljic, Y. Gao, S. Goodarzi, S. Foroughi, and M. J. Blunt (2023c), Pore-scale observations of hydrogen trapping and migration in porous rock: Demonstrating the effect of ostwald ripening, *Geophysical Research Letters*, *50*(7), e2022GL102,383.

Zhao, C.-X. (2013), Multiphase flow microfluidics for the production of single or multiple emulsions for drug delivery, *Advanced drug delivery reviews*, *65*(11-12), 1420–1446.

Figure 1.

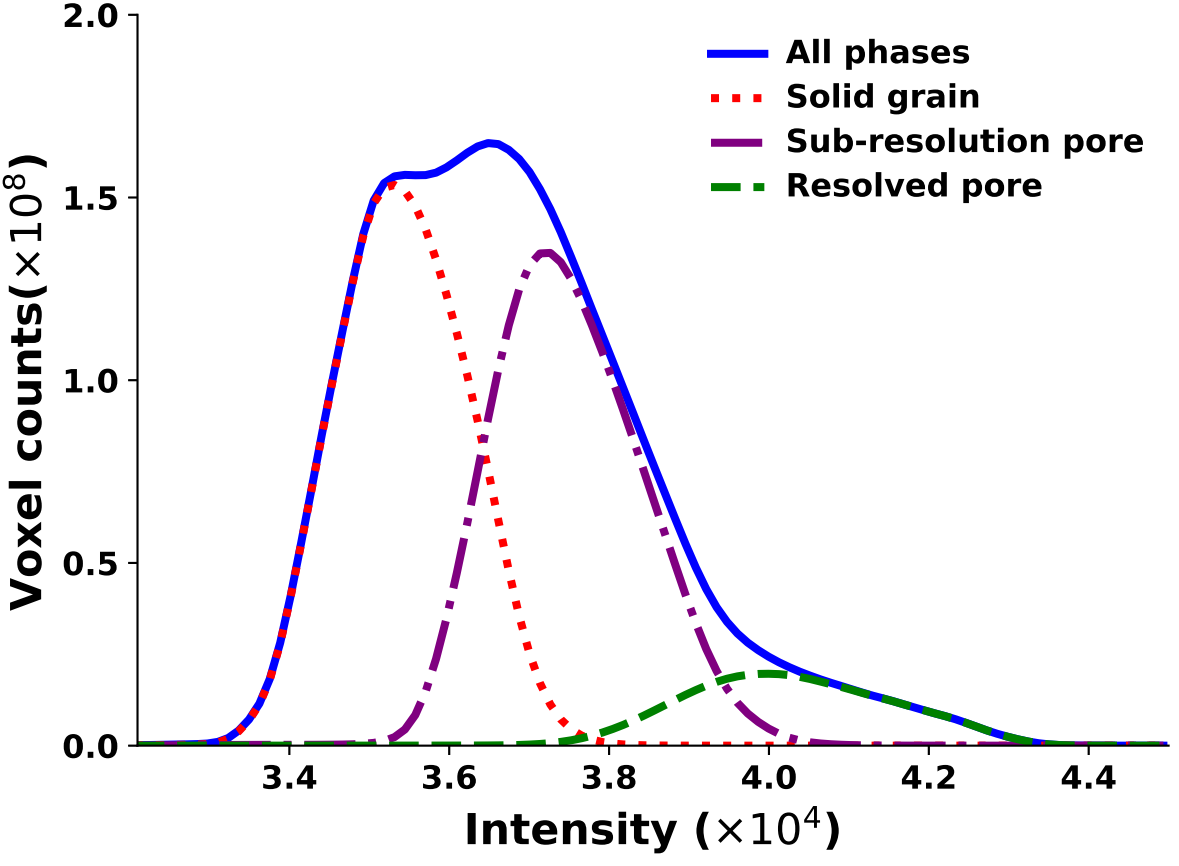
All phases
Solid grain
Sub-resolution pore
Resolved pore
Voxel counts(×10^8)
2.0
1.5
1.0
0.5
0.0
3.4
3.6
3.8
4.0
4.2
4.4
Intensity (×10^4)

Figure 2.

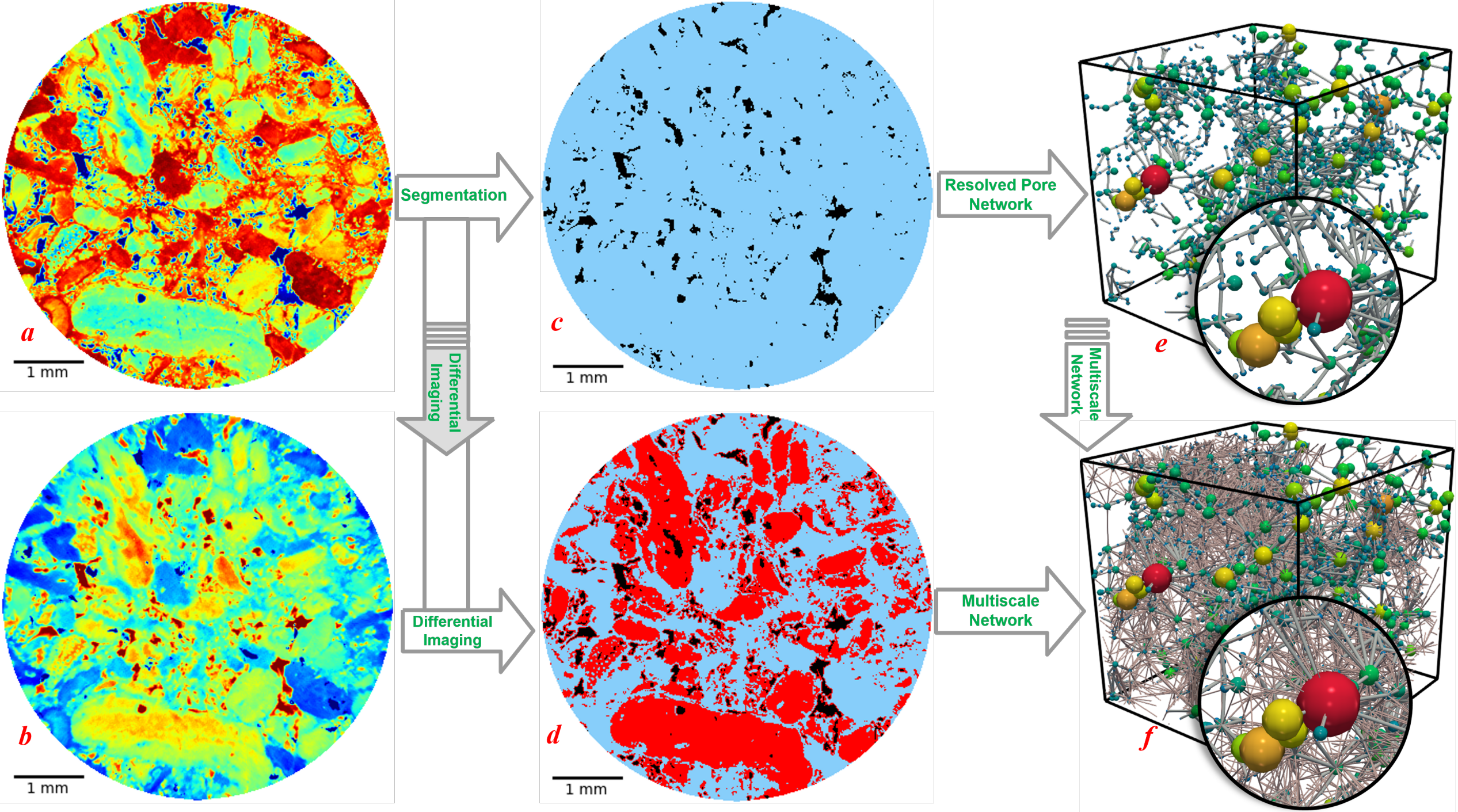
a
1 mm
Segmentation
c
1 mm
Resolved Pore Network
e
Differential Imaging
Multiscale Network
b
1 mm
Differential Imaging
d
1 mm
Multiscale Network
f

Figure 3.

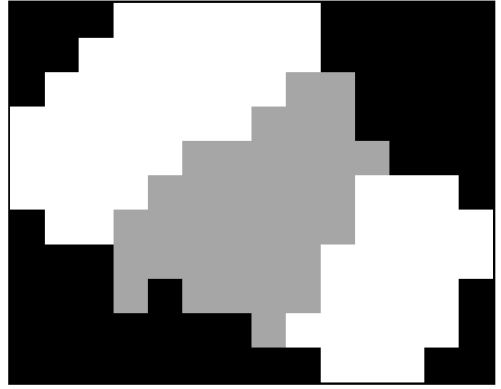

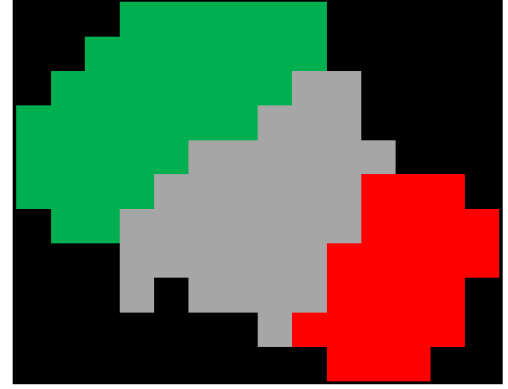

Nearest

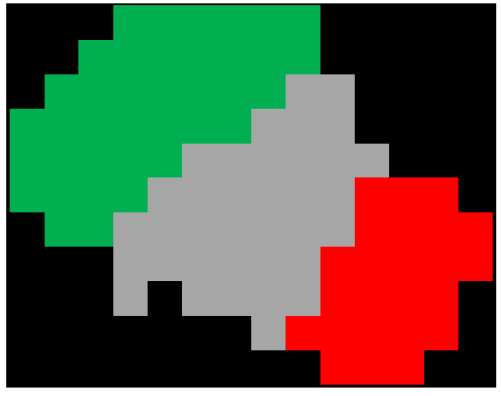

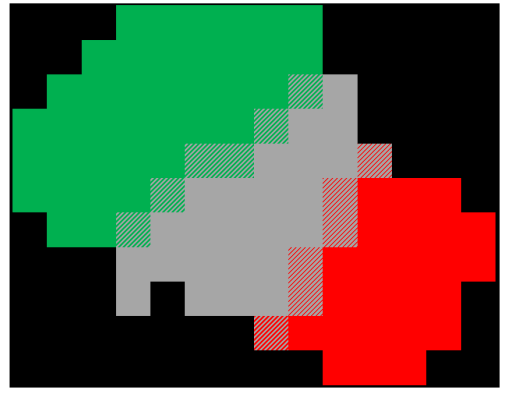

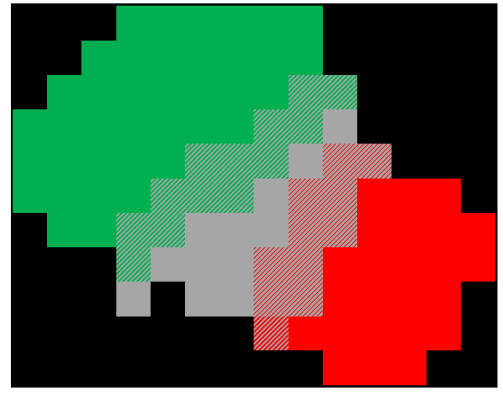

...

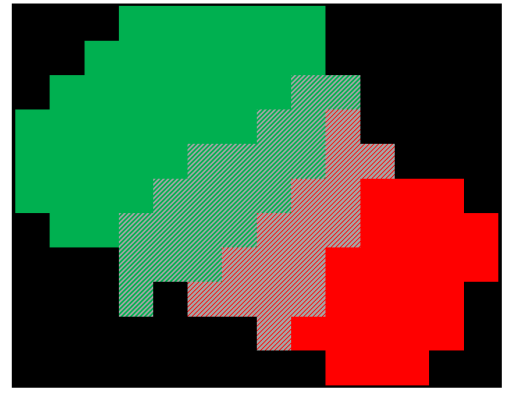

Next-
Nearest

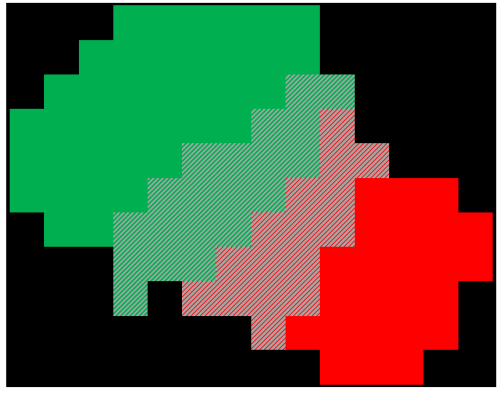

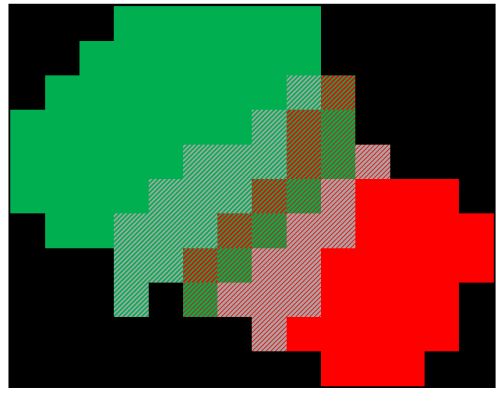

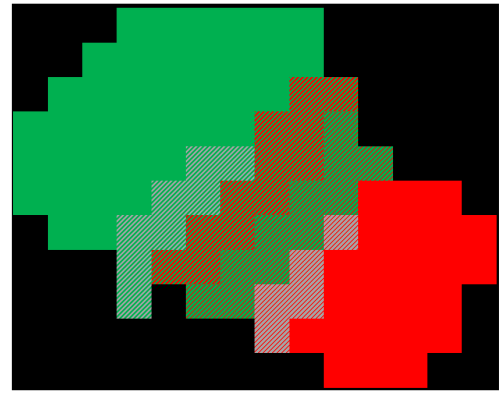

...

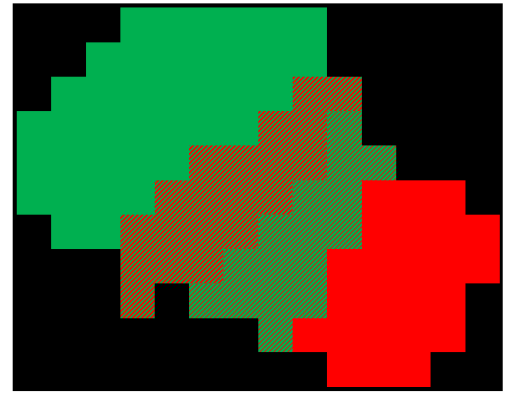

Initial State

1st Dilation

2nd Dilation

Final Dilation

Figure 4.

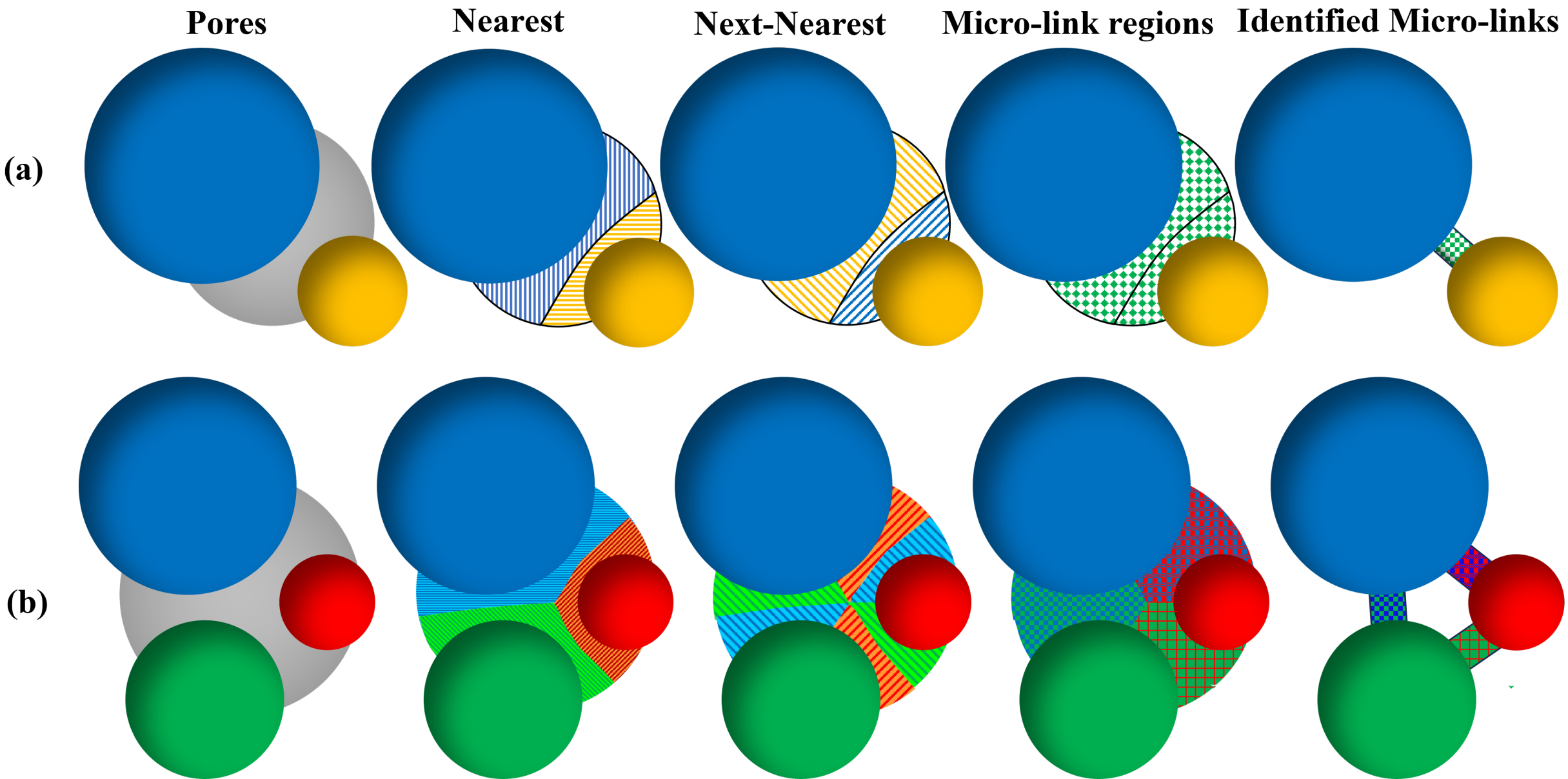
Pores
Nearest
Next-Nearest
Micro-link regions
Identified Micro-links
(a)
(b)

Figure 5.

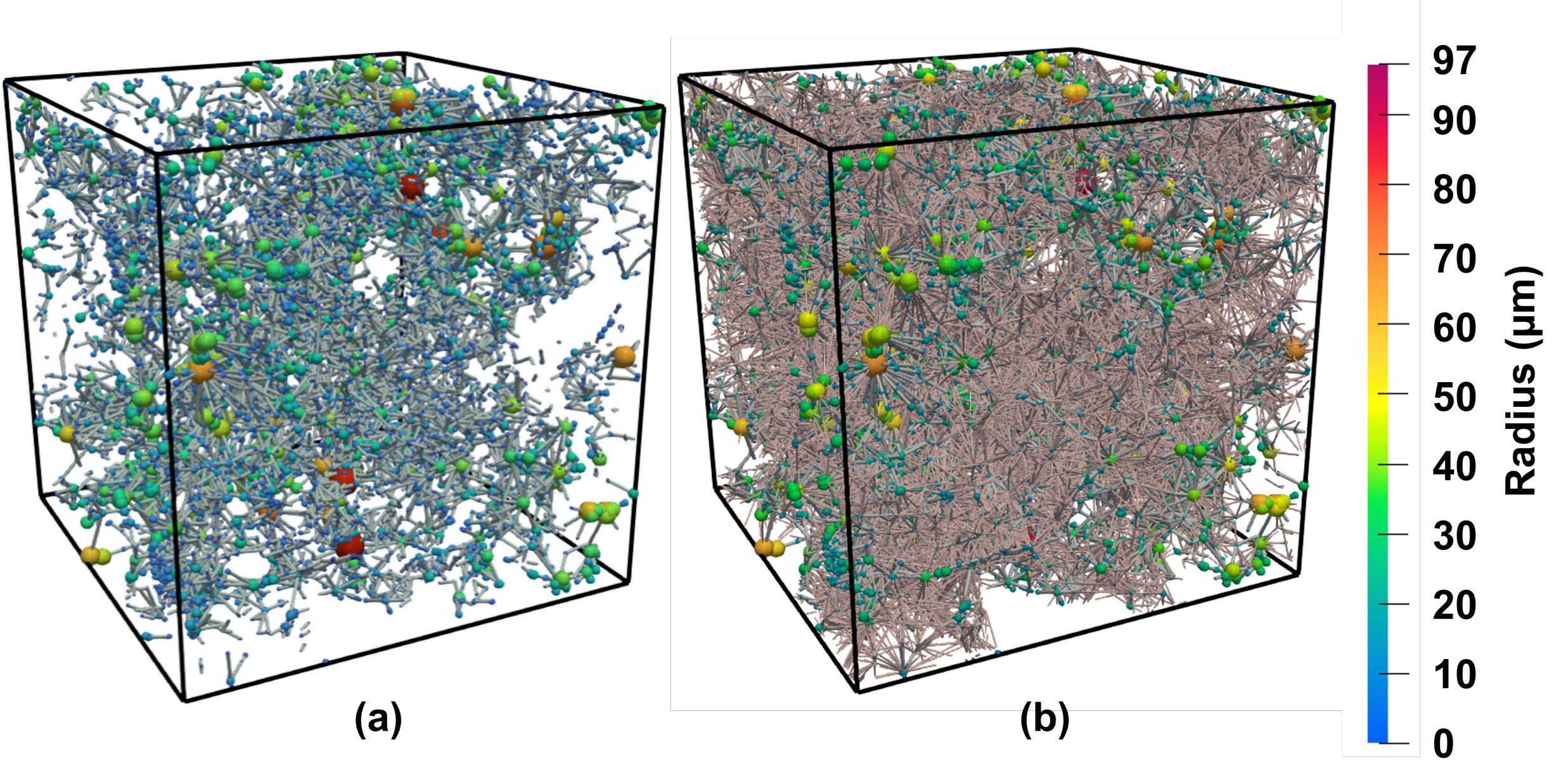
(a)
(b)
97
90
80
70
60
50
40
30
20
10
0
Radius (μm)

Figure 6a.

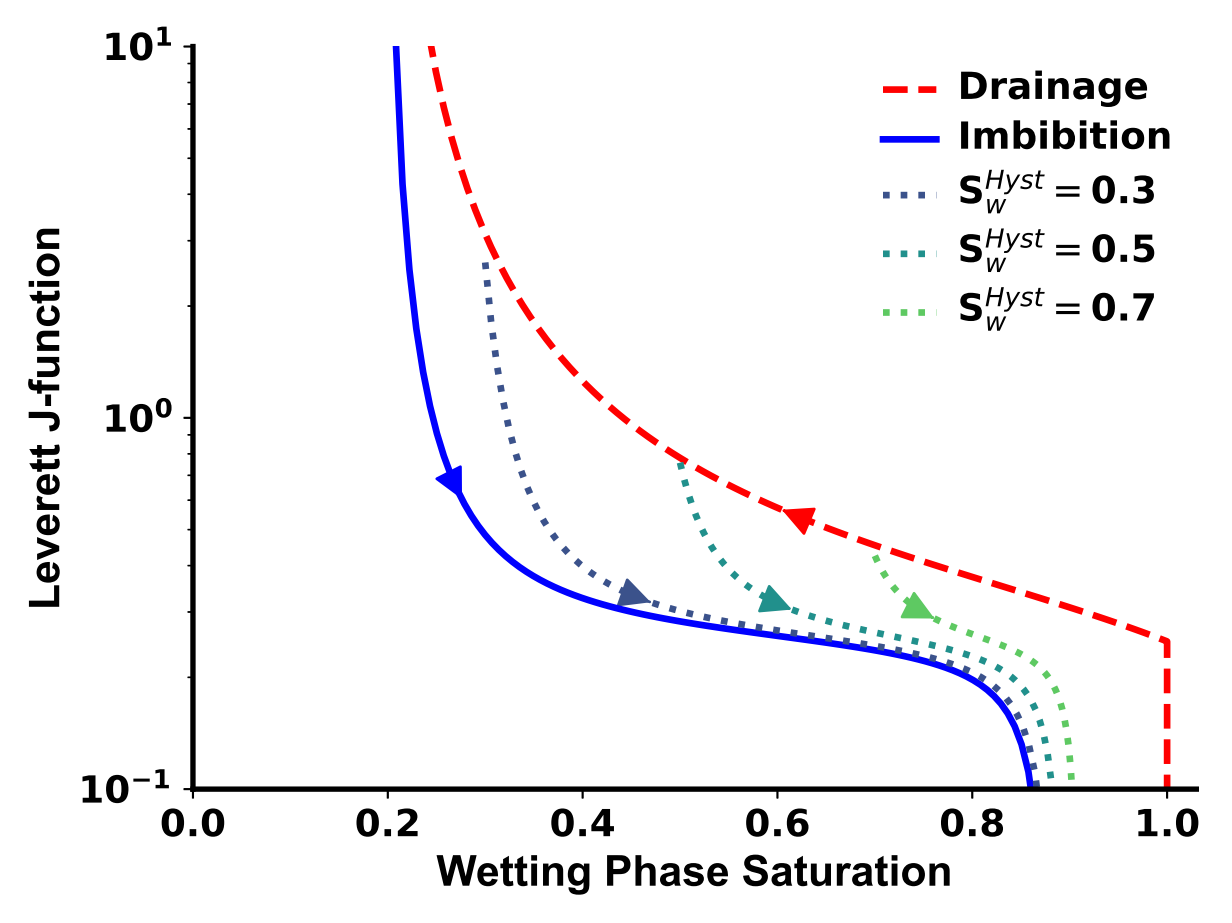
Drainage
Imbibition
$S_w^{Hyst} = 0.3$
$S_w^{Hyst} = 0.5$
$S_w^{Hyst} = 0.7$
Leverett J-function
10^1
10^0
10^{-1}
0.0
0.2
0.4
0.6
0.8
1.0
Wetting Phase Saturation

Figure 6b.

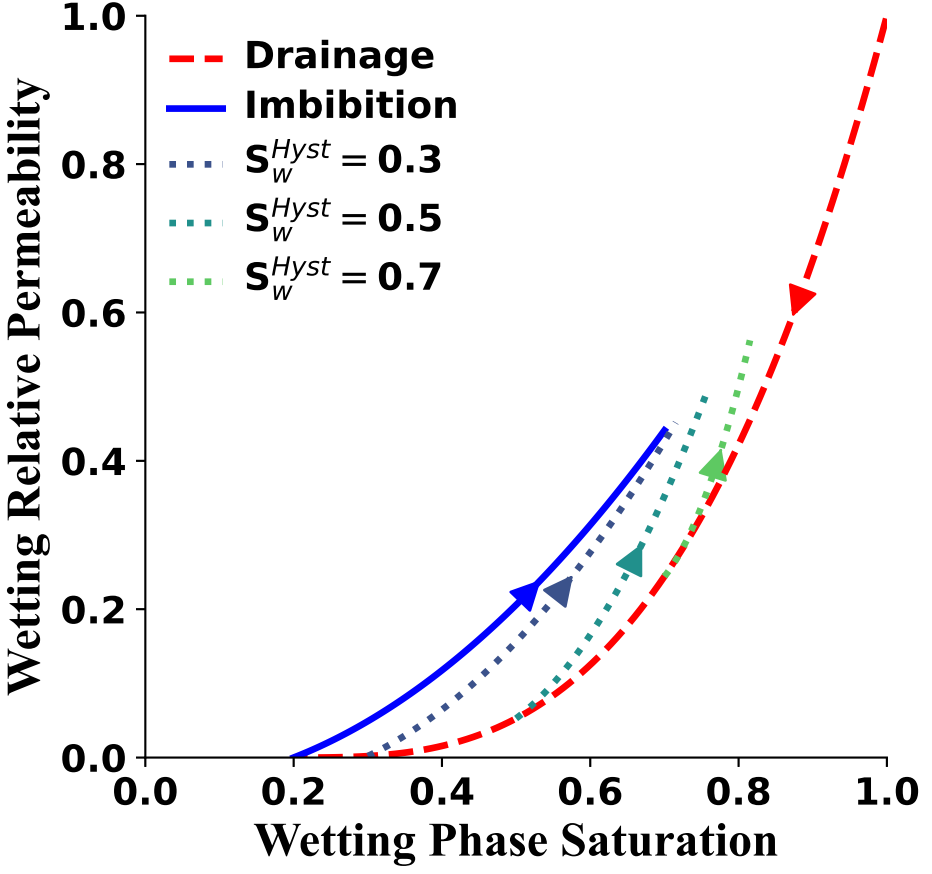
Drainage
Imbibition
$S_w^{Hyst} = 0.3$
$S_w^{Hyst} = 0.5$
$S_w^{Hyst} = 0.7$
Wetting Relative Permeability
Wetting Phase Saturation
0.0
0.2
0.4
0.6
0.8
1.0

Figure 6c.

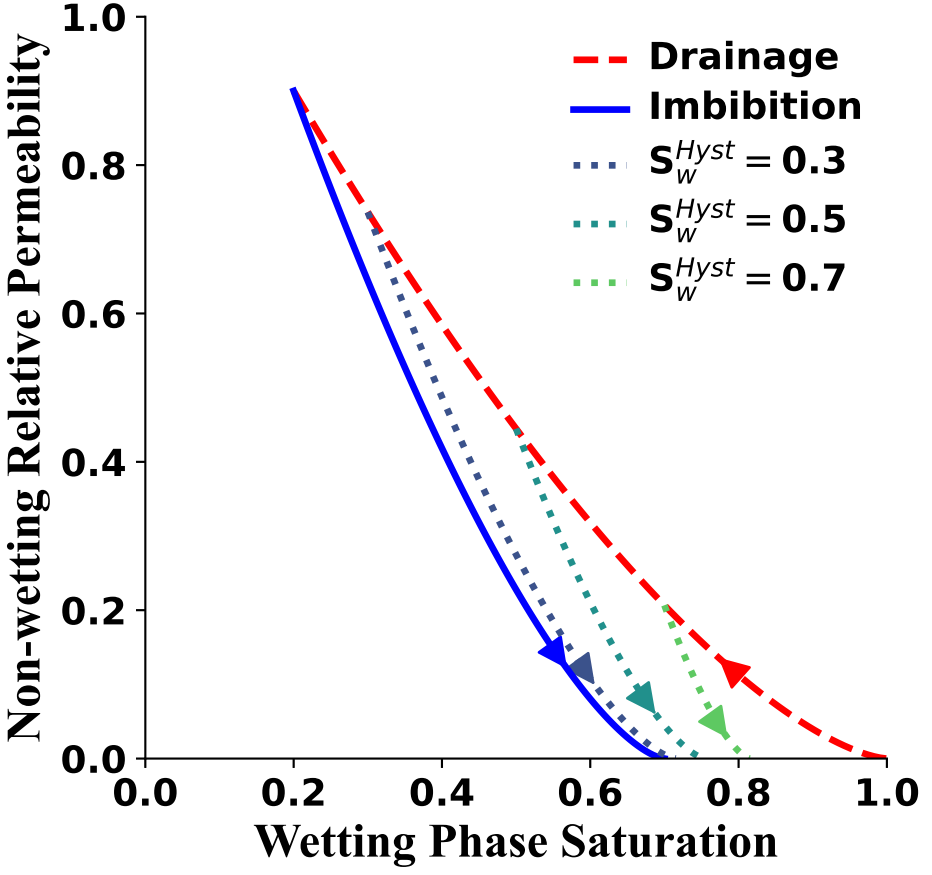
Drainage
Imbibition
$S_w^{Hyst} = 0.3$
$S_w^{Hyst} = 0.5$
$S_w^{Hyst} = 0.7$
Non-wetting Relative Permeability
Wetting Phase Saturation
0.0
0.2
0.4
0.6
0.8
1.0

Figure 7.

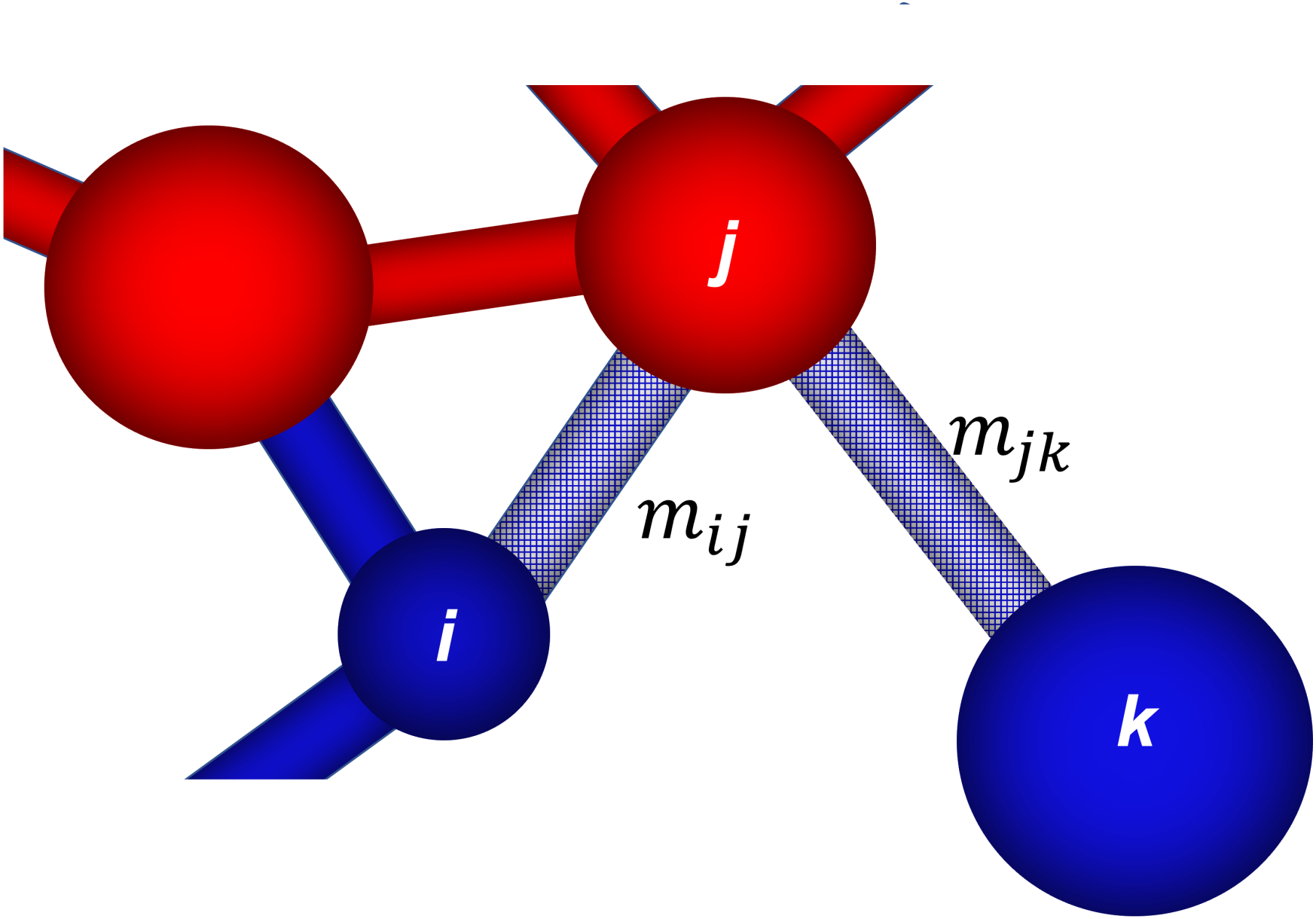
j
i
k
m_{ij}
m_{jk}

Figure 8.

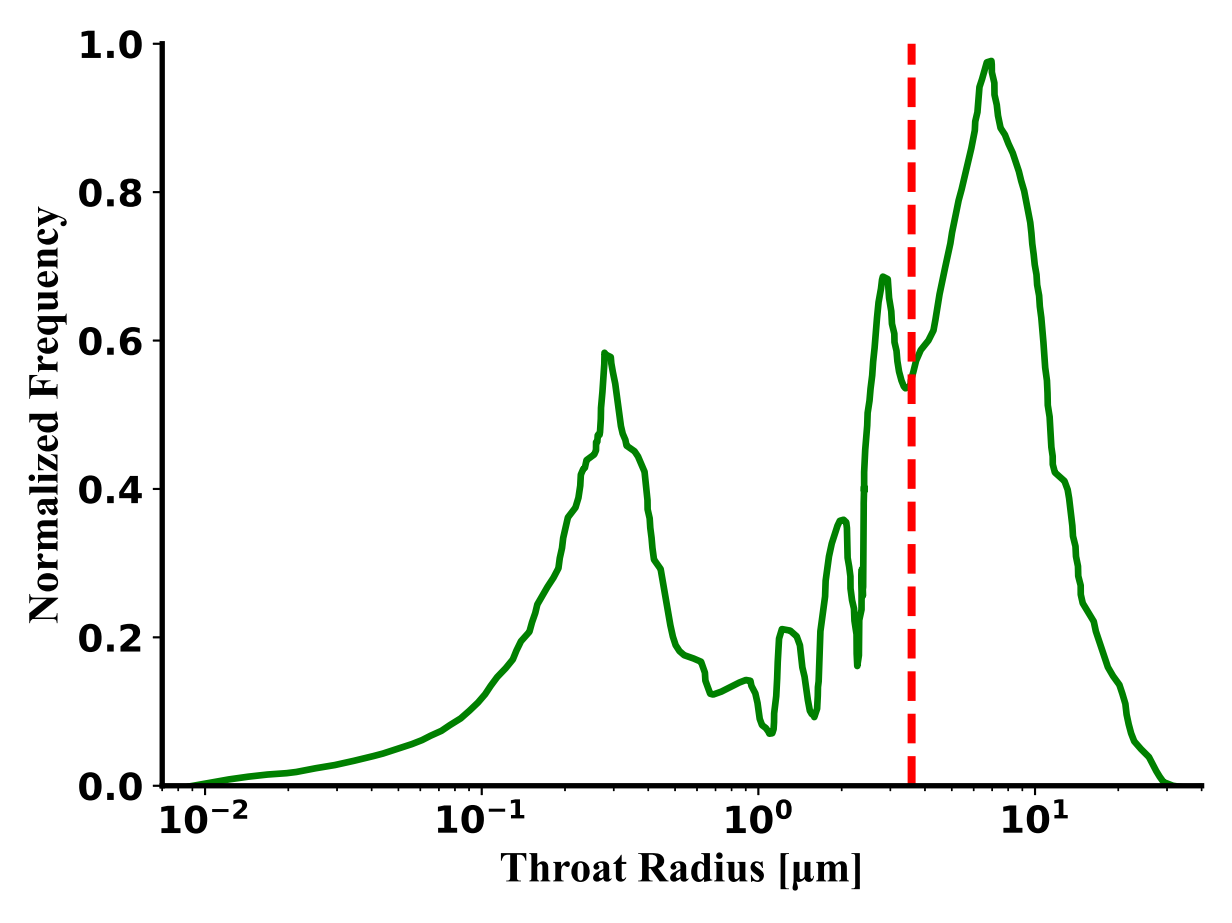
1.0
0.8
0.6
0.4
0.2
0.0
Normalized Frequency
10^{-2}
10^{-1}
10^{0}
10^{1}
Throat Radius [μm]

Figure 9.

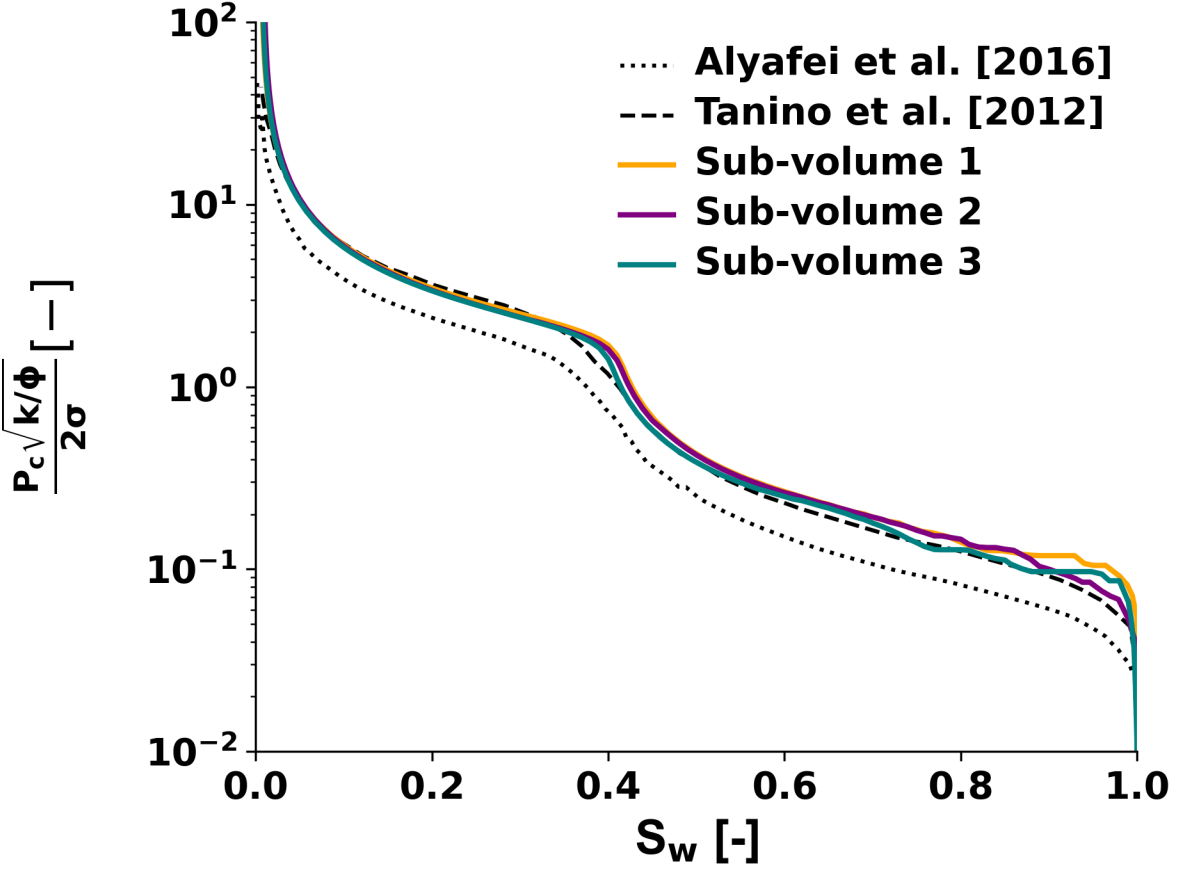
Alyafei et al. [2016]
Tanino et al. [2012]
Sub-volume 1
Sub-volume 2
Sub-volume 3
$\frac{P_c\sqrt{k/\phi}}{2\sigma}$ [−]
10^2
10^1
10^0
10^{-1}
10^{-2}
0.0
0.2
0.4
0.6
0.8
1.0
S_w [-]

Figure 10a.

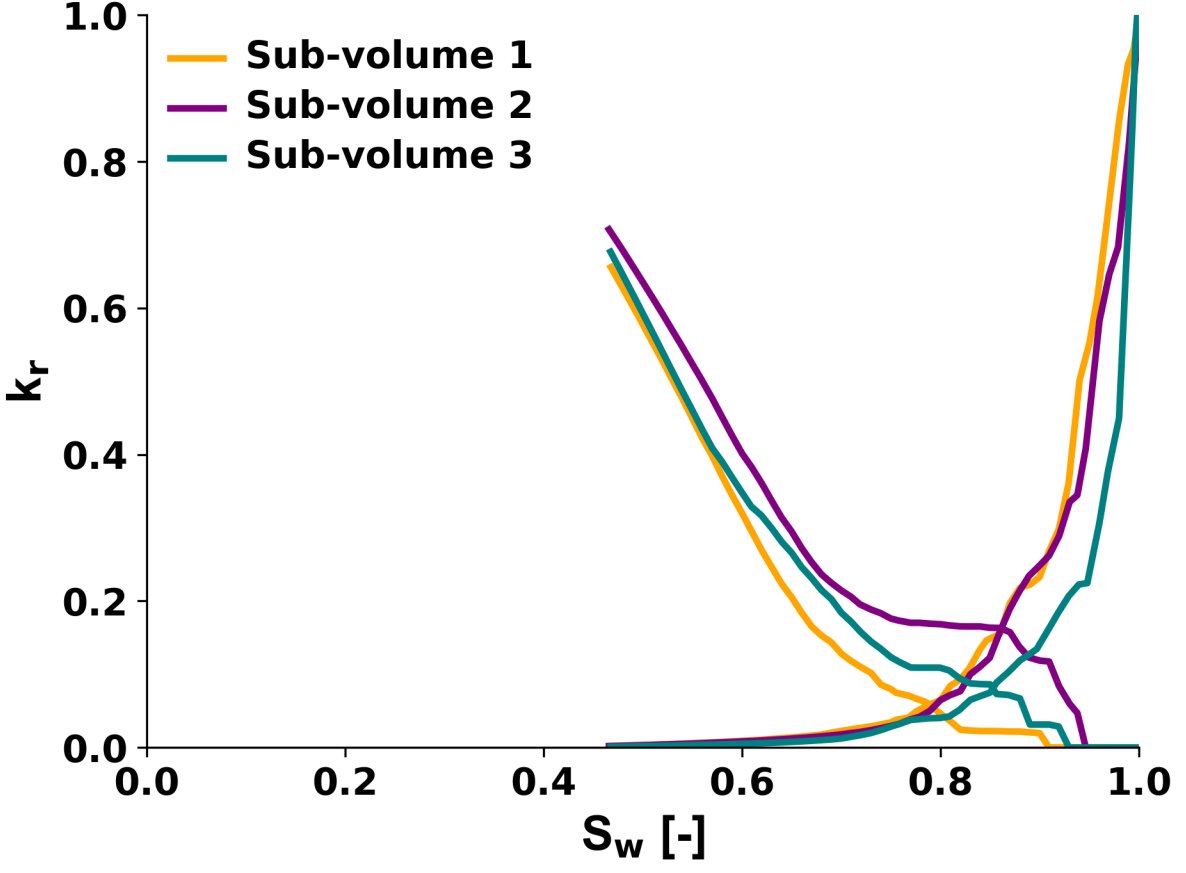
Sub-volume 1
Sub-volume 2
Sub-volume 3
1.0
0.8
0.6
0.4
0.2
0.0
k_r
0.0
0.2
0.4
0.6
0.8
1.0
S_w [-]

Figure 10b.

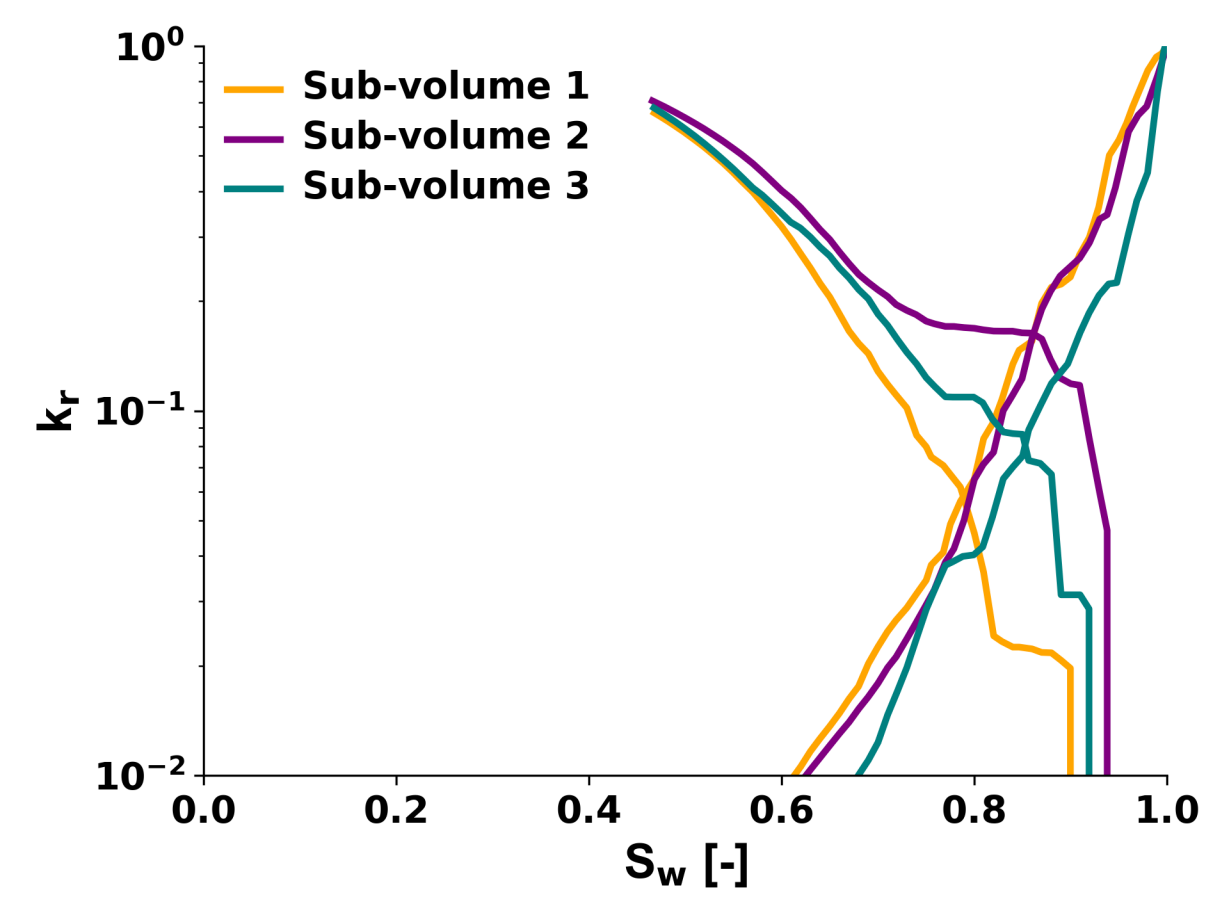
Sub-volume 1
Sub-volume 2
Sub-volume 3
10^0
10^{-1}
10^{-2}
k_r
0.0
0.2
0.4
0.6
0.8
1.0
S_w [-]

Figure 11a.

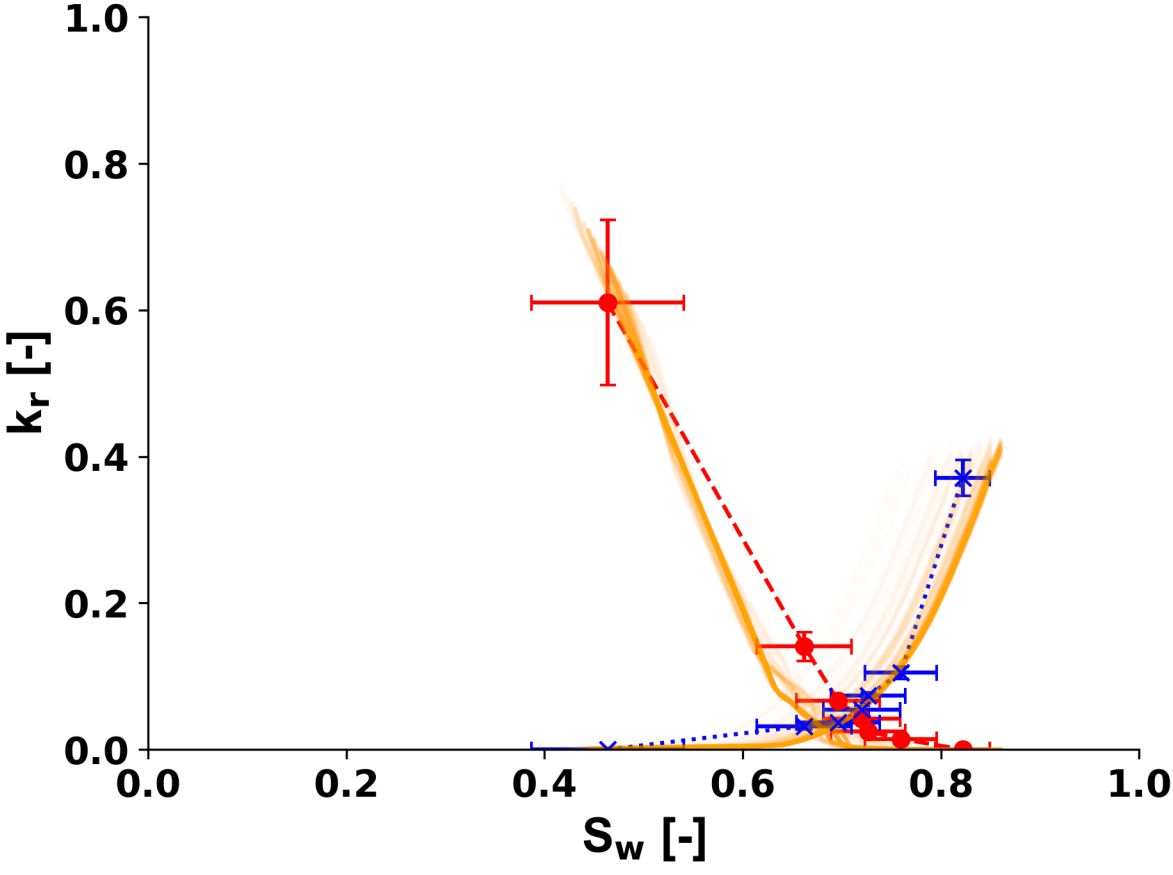
1.0
0.8
0.6
0.4
0.2
0.0
k_r [-]
0.0
0.2
0.4
0.6
0.8
1.0
S_w [-]

Figure 11b.

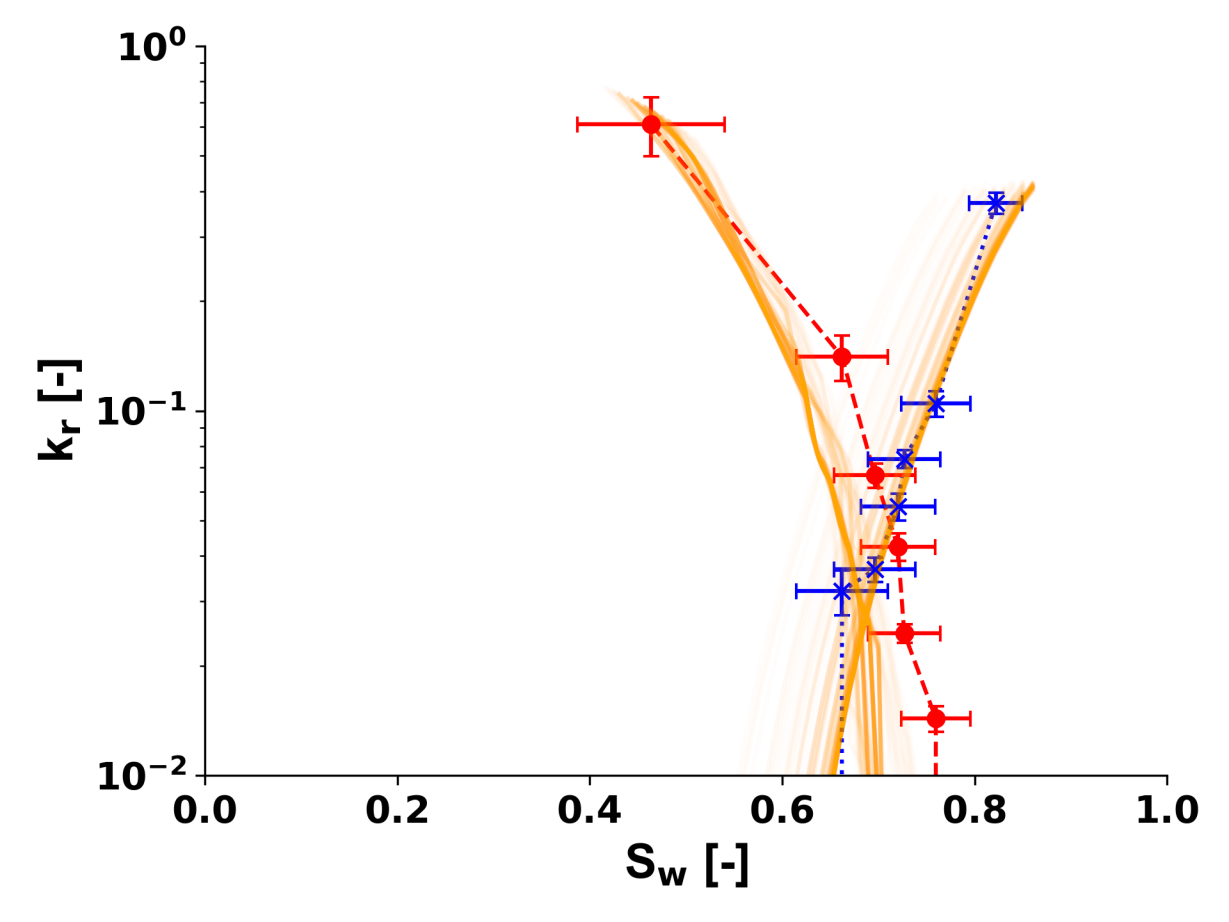
10^0
10^{-1}
10^{-2}
k_r [-]
0.0
0.2
0.4
0.6
0.8
1.0
S_w [-]

Figure 11c.

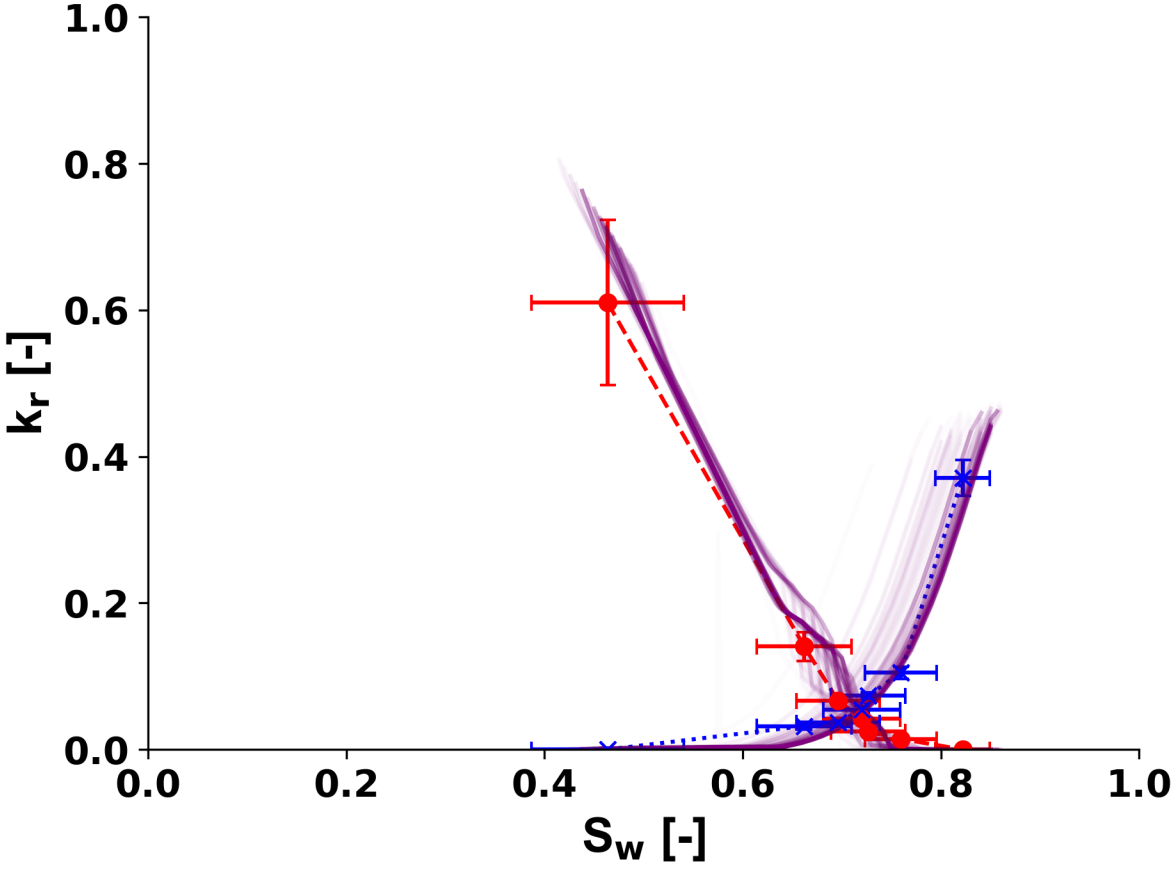
1.0
0.8
0.6
0.4
0.2
0.0
k_r [-]
0.0
0.2
0.4
0.6
0.8
1.0
S_w [-]

Figure 11d.

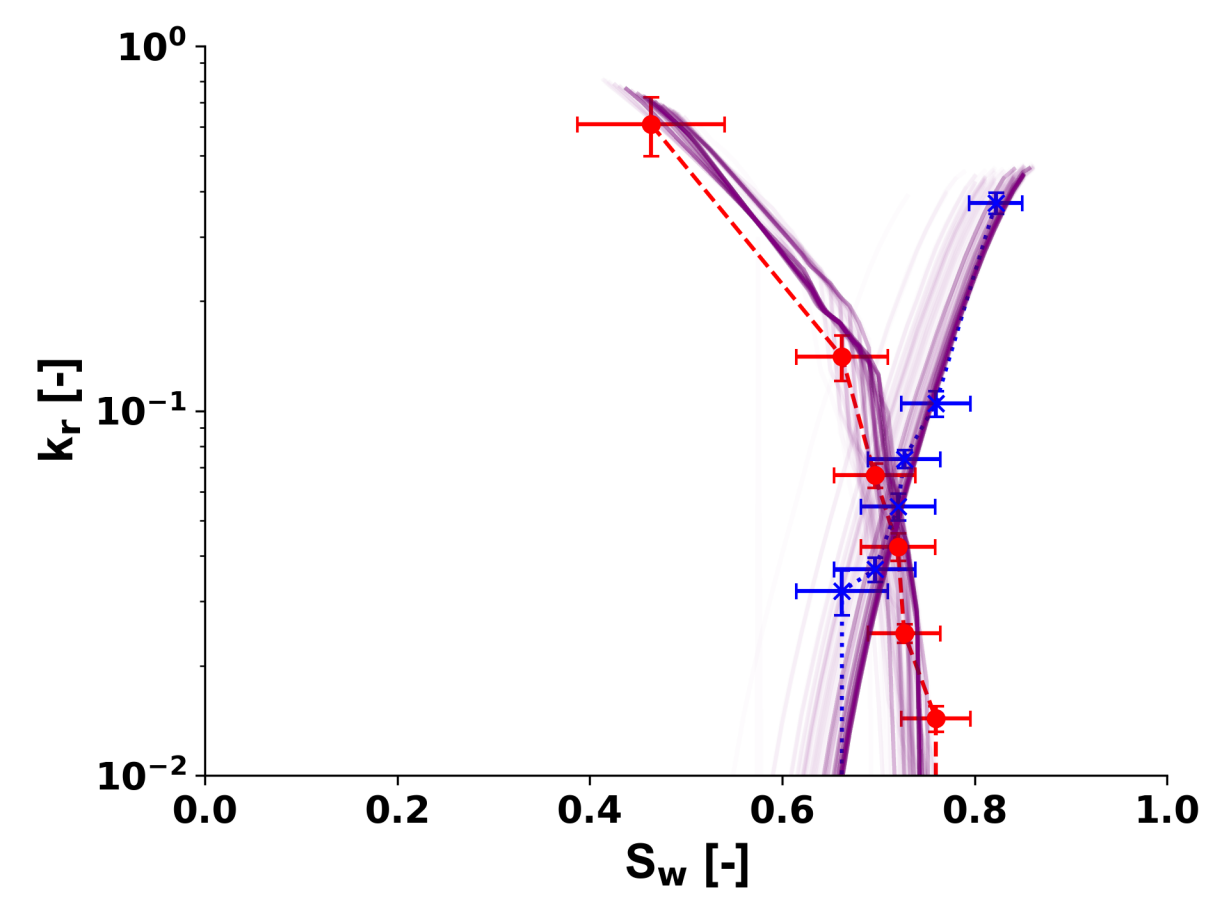
10^0
10^{-1}
10^{-2}
k_r [-]
0.0
0.2
0.4
0.6
0.8
1.0
S_w [-]

Figure 11e.

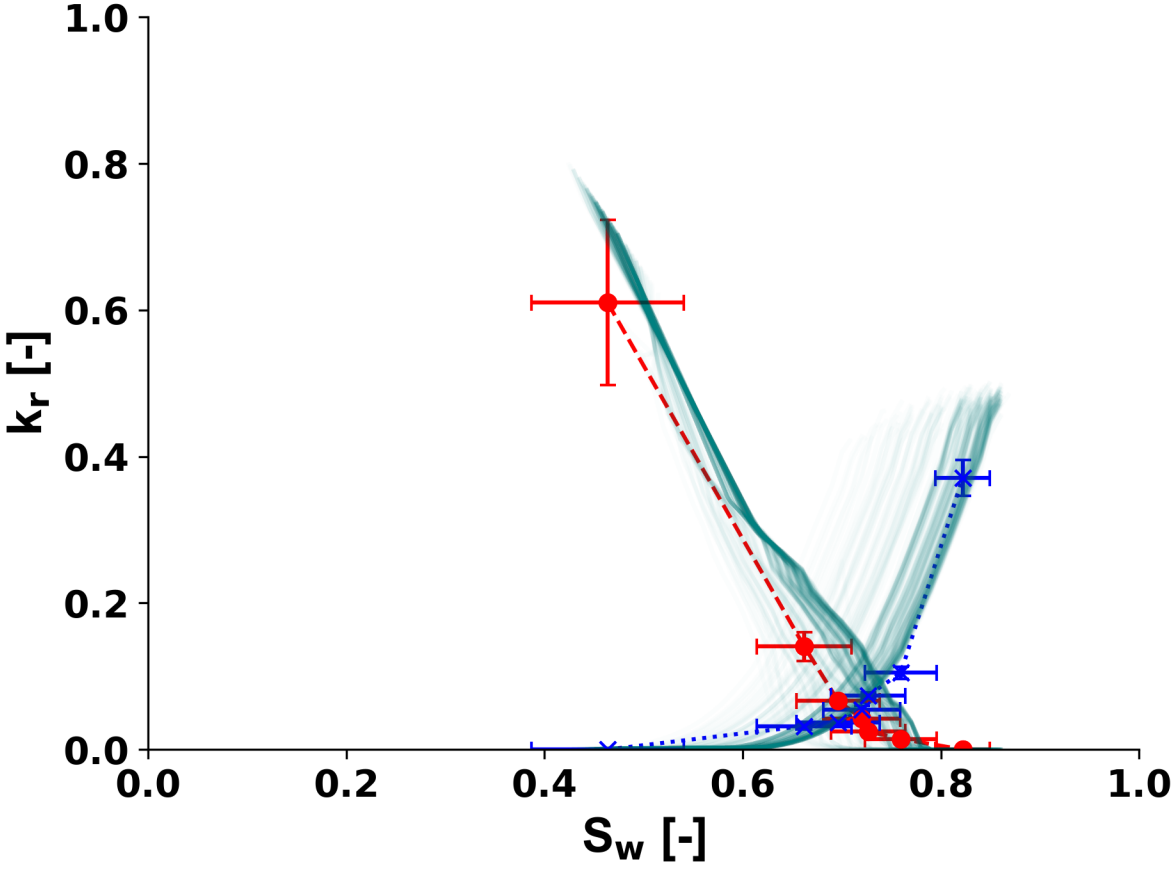
1.0
0.8
0.6
0.4
0.2
0.0
k_r [-]
0.0
0.2
0.4
0.6
0.8
1.0
S_w [-]

Figure 11f.

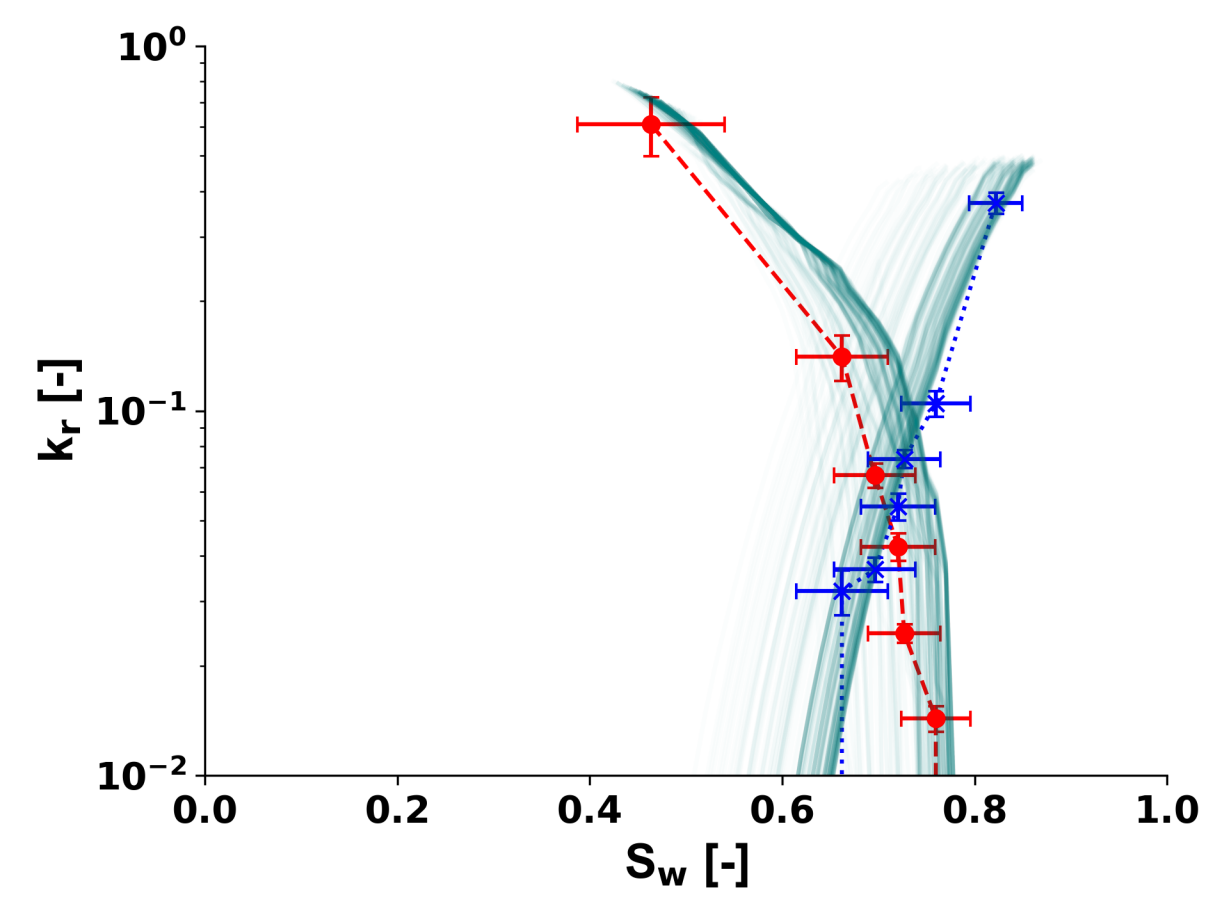
10^0
10^{-1}
10^{-2}
k_r [-]
0.0
0.2
0.4
0.6
0.8
1.0
S_w [-]